Materials Advances

ROYAL SOCIETY OF CHEMISTRY

REVIEW

View Article Online
View Journal | View Issue

Cite this: *Mater. Adv.*, 2023, 4, 3967

High atomic number nanoparticles to enhance spectral CT imaging aspects

Isha Mutreja,[a] Nabil Maalej,[b] Ajeet Kaushik,[cd] Dhiraj Kumar*[e] and Aamir Raja*[f]

Spectral CT imaging (multi-energy detection) is a promising imaging technique that can benefit from the use of high atomic number (high-*Z*) based nanoparticles (NPs) as contrast agents. These NPs can improve image contrast and enable quantitative material reconstruction, potentially leading to more accurate diagnoses and better treatment planning. This article provides an overview of current research on the use of high-*Z* NPs for spectral CT imaging. This briefly covers the physicochemical properties and biocompatibility of eight high-*Z* elements: gadolinium, ytterbium, hafnium, tantalum, tungsten, rhenium, gold, and bismuth. This article also focuses on various *in vitro*, *in vivo*, and simulation studies that have investigated the potential advantages and limitations of using high-*Z* NPs as contrast agents for spectral CT imaging. In addition, the review also highlights the potential preclinical and clinical applications of high-*Z* NPs in cancer diagnosis, therapy, and cardiovascular disease. The emphasis has been on the key outcomes and limitations of prior studies and on identifying potential future research directions and applications for high-*Z* NPs and spectral photon-counting CT imaging. The article concludes by discussing advancements aimed at improving the efficacy and safety of high-*Z* NPs for clinical use, and potential future developments in the field.

Received 12th May 2023,
Accepted 14th August 2023

DOI: 10.1039/d3ma00231d

rsc.li/materials-advances

1. Introduction

Different medical imaging modalities generate organ or tissue images using various sources, such as electrons, light/laser, fluorescence, and electromagnetic energy photons. Modern-day diagnostic techniques that are actively used in clinical or research settings include transmission electron microscopy (TEM), optical coherence tomography (OCT), fluorescence imaging (FL), ultrasonography (USG), positron emission tomography (PET), single photon emission tomography (SPECT), magnetic resonance imaging (MRI), photoacoustic tomography (PAT), computed tomography (CT), and bioluminescence.[1] These modalities are helpful in managing various phases of the diseases, such as cancer, by detecting molecular and cellular markers of different tumor types, mapping disease burden, and monitoring treatment response. Among these modalities, CT is widely used to manage patient diagnostic and treatment progression. In the United States alone, more than 80 million CT scans are performed annually, and this number is expected to exceed 300 million worldwide.[2] Moreover, CT has become a primary tool for cancer imaging, providing accurate tumor staging and follow-up imaging to monitor treatment responses. Therefore, it is one of the most commonly used techniques in disease management and biomedical imaging research.[3]

During a CT scan, a poly energetic beam of X-rays is directed at the patient, and the X-ray tube rotates around the body. The detectors measure the intensity of the X-rays passing through the body from different angles. This information is then processed by a computer using advanced CT reconstruction algorithms. A detailed image of the internal structures or organs inside the body is created to provide a cross-sectional view of the body for diagnosis[4] and interventional procedures such as image-guided biopsies and minimally invasive surgeries.[5] CT imaging provides a quantitative 3D characterization of localized contrast to distinguish the different features of a living system. Modern developments in CT imaging techniques that improve speed, sensitivity/specificity, and resolution have significantly enhanced the ability of users to accurately

[a] *Minnesota Dental Research Center for Biomaterials and Biomechanics (MDRCBB), School of Dentistry, University of Minnesota, 515 Delaware St SE, Minneapolis, Minnesota, 55455, USA. E-mail: imutreja@umn.edu*
[b] *Department of Physics, Khalifa University, Abu Dhabi, United Arab Emirates. E-mail: nabil.maalej@ku.ac.ae*
[c] *NanoBioTech Laboratory, Department of Environmental Engineering, Florida Polytechnic University, Lakeland, FL 33805, USA. E-mail: akaushik@floridapoly.edu*
[d] *School of Engineering, University of Petroleum and Energy Studies (UPES), Dehradun Uttarakhand, India*
[e] *Division of Pediatric Dentistry, School of Dentistry, University of Minnesota, 515 Delaware St SE, Minneapolis, Minnesota, 55455, USA. E-mail: kumard@umn.edu*
[f] *Department of Physics, Khalifa University, Abu Dhabi, United Arab Emirates. E-mail: aamir.raja@ku.ac.ae*

diagnose, treat, and monitor disease response to treatment non-invasively in real-time. It is a powerful tool that goes beyond standard morphological assessments, such as size, shape, and structure, and visualizes multi-dimensional information in a preclinical setting (100 microns or greater voxel) to clinical setting (submillimeter to millimeter) with physiological and pathological significance that is otherwise challenging to decipher. Moreover, the use of nanoparticles in conjunction with spectral CT imaging has opened the door for potential translation to non-invasive molecular imaging at the human scale for the early detection of diseased cells.[6–9]

Spectral CT imaging relies on differentiating energy-dependent information from the CT X-ray scan in the form of linear absorption/attenuation coefficient of tissue, voxel material and/or other components; and concurrently characterizing the tissue and components. During the last two decades, spectral CT imaging has technologically advanced from dual-energy (dual-source or dual-detector, 1st generation) to multi-energy photon-counting (2nd generation).[10] Dual-energy CT (DECT) technologies are advancements in CT imaging technology that have seen significant improvements since the early 2000s to overcome the limitations of traditional imaging technologies. The main principle is to provide a linear attenuation coefficient at two different energies. It can be achieved by using two different X-rays energies: one at low energy (typically 80 keV) and the other at high energy (typically 140 keV). However, the same can be achieved by using a single X-ray source with a dual-layer detection-based technique, which is widely used.[10] One of the key advantages of DECT is its ability to perform material decomposition by combining two energy images to generate material density images. Material decomposition is a process in which different materials within the body are identified and separated based on their unique attenuation properties at different energy levels.[11] DECT imaging is particularly useful for evaluating the brain, chest, abdomen, and pelvis, making it an important diagnostic tool for a range of conditions including cancer, trauma, and infection.[12,13]

Spectral photon-counting CT (SPCCT) is an innovative CT imaging technique that is considered to be the most advanced in the imaging field. This technique combines the use of conventional X-rays within the diagnostic energy range (30–140 keV). The SPCCT system incorporates specialized photon-counting detectors (PCDs) that are designed to measure and process the energy signatures of individual incoming photons as well as the signatures of specific atoms/elements – a process commonly referred to as the K-edge photoelectric effect. By utilizing the PCDs, the SPCCT system enables the acquisition of multiple energy-resolved images simultaneously, thereby significantly enhancing imaging capabilities. This approach provides valuable and detailed information about the composition of various elements.[10,14–18] One of the main advantages of SPCCT is its ability to perform material identification and quantification of different materials based on their density, atomic composition, and energy-dependent attenuation. Unlike conventional CT or even DECT systems, SPCCT can effectively distinguish between different contrast agents with similar X-ray attenuation properties. Therefore, the development of new contrast agents that can generate distinctive spectral signatures is not only crucial for the further advancement of SPCCT, but the use of targeted contrast agents that bind to specific molecules or receptors can also provide information on the expression and distribution of site-specific targets, enabling the visualization of molecular and cellular processes.[19] This can have significant clinical applications, such as in the detection and characterization of tumors and the assessment of therapeutic response.[20,21]

Moreover, SPCCT imaging improves traditional CT imaging by detecting and quantifying distinct K-edge energies of high-atomic-number (high-Z) elements in the targeted region.[22] High-Z elements absorb X-rays more strongly than other elements commonly found in the body such as carbon, oxygen, nitrogen, and calcium. This leads to greater contrast between the high-Z elements and the surrounding tissues, including bone, making it easier to distinguish between different structures/organs/biological components in the body. These new K-edge or element energies of the selected elements are presented as colorized voxels against a standard X-ray background.[23] The advantage of SPCCT over traditional CT imaging is its ability to isolate signals at the molecular level for molecular imaging. This property helps to overcome the relatively low inherent contrast within soft tissues.[23,24] Consequently, SPCCT achieves better image contrast, higher spatial resolution, reduced radiation dose, and enhanced diagnostic accuracy, thereby reducing exposure to ionizing radiation.[25–28]

In general, high-Z NP studies for contrast agent development involve several important stages (Fig. 1A). First, the material for high-Z NPs and its synthesis technique must be selected with the desired properties such as shape, size, electrical, and optical properties in mind. It is also important that the NP surface be functionalized to achieve better targeting, better blood circulation, and biocompatibility. Surface modifications include covalent and non-covalent functionalization, encapsulation, and ligand exchange. After surface modification, the properties of the functionalized NP should also be characterized. The next stage is to test the high-Z nanoparticles in a phantom to determine if the NPs provide high contrast at sufficiently low concentrations to avoid toxicity. *In vitro* cell culture studies with healthy and cancer cells are required to verify cell targeting and determine cell viability at the required NPs concentration for contrast enhancement. Finally, animal studies are required to determine whether passive or active targeting of the NPs achieves sufficiently high concentration in the target tissue to achieve a perceivable contrast and to study the pharmacokinetics and toxicity of NPs contrast agents. Only after successful completion of the cell culture and in animal studies that the NPs testing can proceed to test in humans. Fig. 1B represents some sample images collected during research and clinical investigation using traditional (clockwise direction: FL, PAT, and US scans of tumors in mouse models, PET-CT scans of the human body, and MRI scans of mice showing different organs) and spectral photon-counting CT imaging technologies (clockwise direction: gold nanoparticles, yellow color in the lungs, gadolinium, green color – stomach and intestines, and iodine,

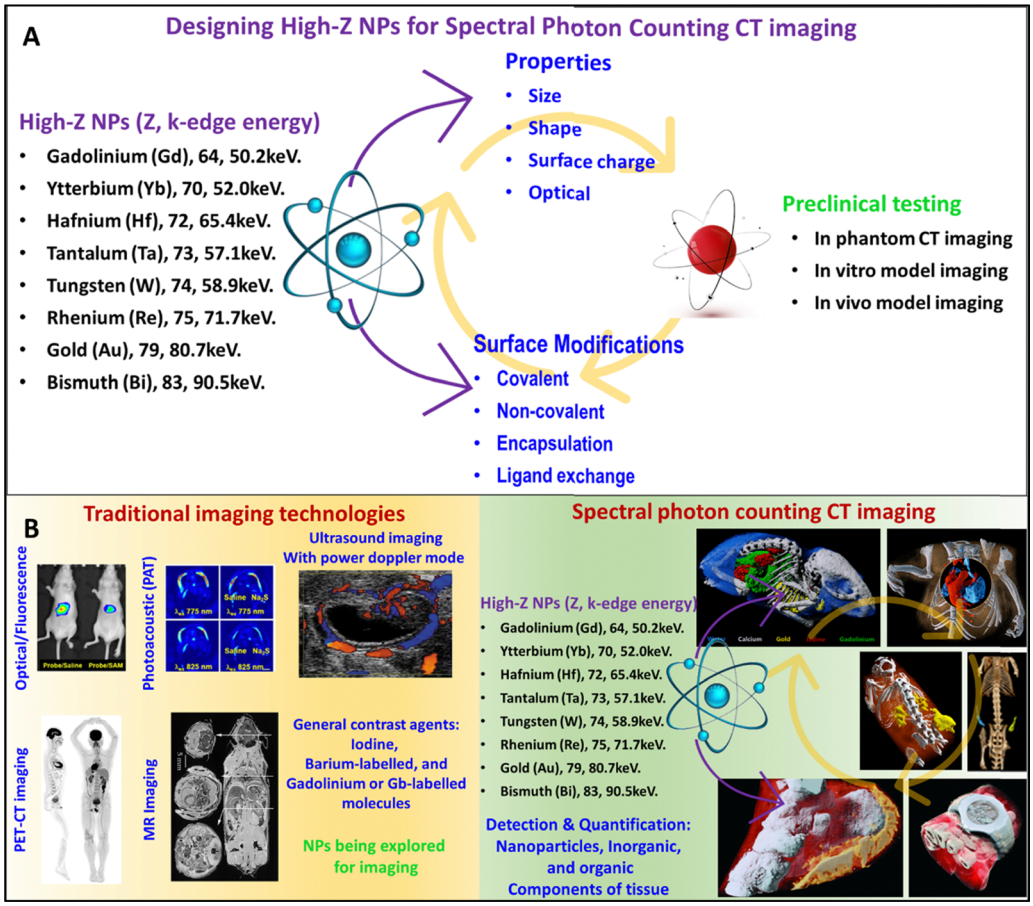

Fig. 1 Stages of development of high-*Z* NPs X-ray contrast agents. The stages include synthesis, characterization, surface modification of high-*Z* NPs followed by in phantom, *in vitro*, and *in vivo* testing/studies using small and large animal models (A). Representative image of research and clinical scans using traditional (clockwise direction: FL, PAT, and US scans of tumors in mouse models, PET-CT scan of human body, and MRI scan of mouse showing different organs) and advanced SPCCT technologies (clockwise direction: gold nanoparticles, yellow color in the lungs, gadolinium, green color – stomach and intestines, and iodine, red color – bladder and kidneys while soft tissue and bone in blue and white colors respectively-MARS bioimaging, mouse heart, and surrounding tissue, Yb and Au nano colloid in blue and yellow in the mouse model, and AuNPs as yellow color in kidney and tumor in mouse model-MARS bioimaging, and very first human wrist with a watch scan, & human ankle-MARS bioimaging) (B). Reproduced from ref. 29–36 with permission from American Chemical Society (copyright 2019), International Institute of Anticancer Research (copyright 2013), The Society of Nuclear Medicine and Molecular imaging (copyright 2019), Radiological Society of North America (copyright 2002), MARS bioimaging Ltd, New Zealand, and American Society of Chemistry (copyright 2022).

red color – bladder and kidneys while soft tissue and bone in blue and white colors respectively – MARS bioimaging, mouse heart and surrounding tissue, Yb and Au nano colloid in blue and yellow in the mouse model, and AuNPs as yellow color in kidney and tumor in the mouse model – MARS bioimaging, and very first human wrist with a watch scan, & human ankle – MARS bioimaging).[29–36]

However, the use of high-*Z* nanoparticles as contrast agents in imaging presents several challenges, including toxicity, rapid clearance, and retention in tissues. These challenges are especially important for clinical applications where high doses of the NP agent may be necessary to achieve sufficient contrast enhancement. Small NPs can be cleared quickly, which reduces the imaging sensitivity and limits the imaging time window. However, larger NPs may accumulate in organs such as the liver and spleen, which can cause tissue damage, inflammation, and other adverse effects.[37,38] To overcome these challenges, it is essential to optimize the size, shape, surface coating, and dosing of the high-*Z* NPs before use in animals or humans.[39] Additionally, high-*Z* NPs can be synthesized in optimal sizes, and shapes, and functionalized with biocompatible coatings to improve their retention in the body and reduce toxicity. With the optimization of these physico-chemical properties of nanoparticles, the cell-nanoparticle interaction can be controlled to guide the cellular or tissue uptake of nanoparticles by known mechanisms such as phagocytosis, clathrin-mediated endocytosis, caveolae-dependent endocytosis, micropinocytosis and others (diffusion, microinjection, and hole formation).[40–48] For instance, biocompatible polymer coating has been shown to significantly reduce the toxicity of gold NPs.[49,50] Therefore, in this review, we systematically collate the latest advances in the last decade, in which high-*Z* nanoparticulate systems have been used for contrast enhancement in DECT and SPCCT. This review focuses on covering studies focused on the utilization of

high-Z NPs in *in vitro*, *in vivo*, and simulation research studies and delineates potential future developments. We also discussed the potential clinical benefits and limitations of using high-Z NPs as X-ray contrast agents.

2. Principle of spectral CT imaging using high-Z nanoparticles (high-Z NPs)

For decades, iodine-based contrast agents have been used to enhance the contrast between blood vessels and blood pools. However, a known side effect of iodine-based contrast agents is that they can cause allergic reactions in some patients. Furthermore, renal malfunction has been reported, particularly in patients with renal insufficiency. This risk is known as contrast-induced nephropathy (CIN) or contrast-induced acute kidney injury (CI-AKI) and can cause reduced kidney function.[51] Moreover, the K-edge of iodine (33 keV) is towards the low-energy spectrum of the diagnostic imaging energy spectrum, which is subject to high photon absorption and hence, beam hardening. As a result, low-energy photons are mostly absorbed by patients, thereby increasing radiation exposure. This has prompted researchers to develop and investigate alternative high-Z elements as contrast agents.[52]

High-Z NPs have emerged as promising contrast agents for SPPCT imaging owing to their unique physical and chemical properties. In particular, they have been explored as promising contrast agents for DECT and SPCCT, advanced imaging modalities. These imaging technologies can enhance the contrast, and material composition of tissues by detecting and quantifying the distinct K-edge energies of high-Z elements in a targeted region. Many high-Z elements have been suggested as alternative elements for spectral CT imaging due to their ability to attenuate X-rays in the diagnostic energy range such as europium (Z = 63; K-edge = 48.5 keV), gadolinium (Z = 64; K-edge = 50.2 keV), terbium (Z = 65; K-edge = 52 keV), ytterbium (Z = 70; K-edge = 61.3 keV), hafnium (Z = 72; K-edge = 65.3 keV), tantalum (Z = 73; K-edge = 67.4 keV), tungsten (Z = 74; K-edge = 69.5 keV), rhenium (Z = 75; K-edge = 71.6 keV), gold (Z = 79; K-edge = 80.7 keV), and bismuth (Z = 83; K-edge = 90.5 keV). Fig. 2 shows the simulated mass attenuation coefficients of several high-Z NPs and their respective K-edges.[49] Some of these high-Z NPs not only serve as contrast agents for imaging but also have therapeutic properties, allowing for targeted treatment of certain diseases or conditions. For example, gold nanoparticles have been investigated for their potential as both contrast agents and targeted drug delivery agents.[53] By introducing high-Z NPs or hybrid high-Z NPs (mixed with Fe) at the disease site through passive or active targeting, the image contrast of targeted tissues can be enhanced, and the diagnostic accuracy of advanced and conventional imaging modalities can be improved.[54–56]

High-Z materials have K-edge energies within a diagnostic imaging energy range, where there are a reasonable number of photons above and below their K-edge (approximately 40–100 keV in a 120–140 kVp beam) as shown in Fig. 2A. Gold and bismuth have the highest Z and hence the highest attenuation coefficient at their respective K-edges. In an SPCCT system, the energy ranges of the photon-counting detectors can be adjusted to capture the sudden increase in X-ray attenuation of the elements.[58] For instance, for a gold K-edge of 80.72 keV, setting an energy window immediately below and above the K-edge would result in a large difference in X-ray attenuation by high-Z NPs.[59] Moreover, multi-energy windows provide users with the opportunity to set up energy windows in the low-energy photoelectric region. In general, the photoelectric and Compton effect are the primary mechanisms by which materials attenuate X-ray beams in the diagnostic energy range. Generally, in the photoelectric effect, a K-shell electron receives energy owing to a collision with a photon, which transfers its energy to the electron, leading to its ejection from its shell and traveling a short distance before its energy is lost. The photoelectric effect is scaled with Z^3 for any given photon energy, which means that iodine (conventional contrast agent) is likely to produce 2.6- and 3.8-times smaller X-ray contrast than that of

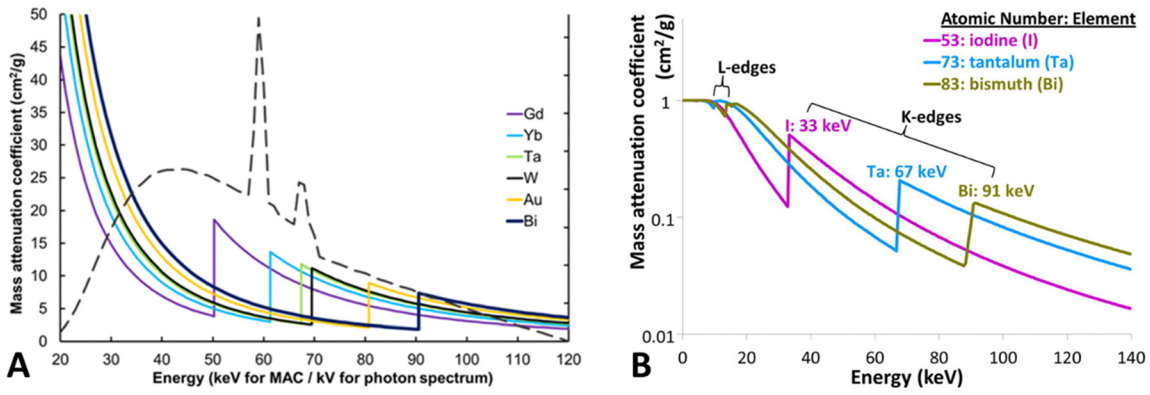

Fig. 2 Mass attenuation coefficients of several high-Z materials as a function of energy. Also showing a tungsten X-ray spectrum for 120 kVp tube peak voltage. Reproduced from ref. 51 with permission from by the authors, Licensee: Springer Nature, under the Creative Commons Attribution License, copyright 2018. The logarithmic mass attenuation coefficient emphasizes how the attenuation effect varies with energy and K-edge (B), reproduced from ref. 57 with permission from Elsevier B.V., copyright 2016.

tantalum (Z = 73) and bismuth (Z = 83), respectively compared to iodine K-edge. However, the photoelectric effect is inversely proportional to the energy of the photon cubed ($1/E^3$) and decreases as the energy increases. Consequently, tantalum and bismuth generate 8.1- and 20.2-times lower contrast respectively, compared to iodine due to their higher K-edge energy (Fig. 2B). This inverse relationship with energy could significantly negate the greater attenuation benefit from the high atomic number at higher energies. K-edge energy imaging can be used for the detection and differentiation of diverse elemental densities. Previous reports have demonstrated the effectiveness and potential application in quantitative measurements and differentiation of Ta and I during a phantom study using SPCCT.[60] Such an analytical tool for region-of-interest (ROI) offers opportunities for diagnosing site-specific irregularities as a result of diseased tissue or blockage.

Moreover, a few studies have also indicated that elements with Z numbers in the range of 63–73 can be considered optimal for enhancing spectral X-ray contrast efficiency, while higher Z elements may decrease photon counts sensed by the detectors and increase the crosstalk between bone and other surrounding soft tissues.[2,51,61] In addition to the X-ray attention of high-Z NPs, other properties need to be considered, that includes biocompatibility, non-toxicity, ease of synthesis and tuning of sizes and shapes, ease of surface functionalization for cell targeting, favorable pharmacokinetics, and low cost.[51]

3. Gold (79) nanoparticles

Gold nanoparticles (AuNPs) exhibit several properties that favor them over other nanomaterials. It has a high atomic number (Z = 79) and high K-edge energy (80.7 keV) in the diagnostic imaging energy range. It also has an X-ray mass attenuation coefficient of 5.16 $cm^2\ g^{-1}$ at 100 keV energy and provides 2.7 times greater contrast than iodine (1.94 $cm^2\ g^{-1}$). Additionally, the ease of AuNP synthesis (Fig. 3A) and ability to functionalize the synthesized nanostructures with different functional molecules (Fig. 3B), along with their biocompatibility and low toxicity, make them good candidates for biomedical applications. They also demonstrated the size- and shape-dependent optical and electronic properties.

The literature provides strong evidence that AuNPs smaller than 100 nm have been favored for different clinical applications, especially cancer cell targeting, imaging, and therapy in humans and animals.[62] This influx of AuNPs has been linked to biocompatibility, nontoxicity, and longer blood or lymphatic circulation times.[64] In a recent *in vitro* study, the MARS SPCCT scanner was used to show the selective uptake of monoclonal

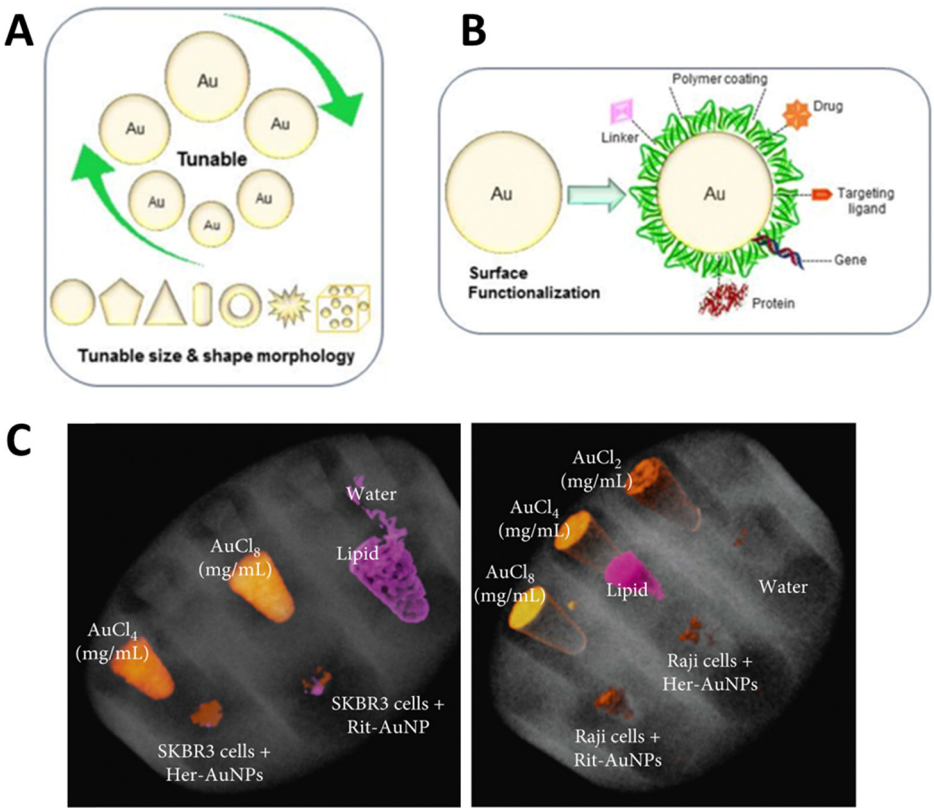

Fig. 3 Important properties of AuNPs (tunable size and shape) (A), ease of surface functionalization (B), reproduced from ref. 62 with permission by the authors, Licensee: MDPI, Basel, Switzerland, under the Creative Commons Attribution License, copyright 2018, and SPCCT imaging of different concentrations of gold and AuNP-herceptin binding to HER2-positive breast cancer cells (SKBR3) (C), reproduced from ref. 63 with permission by the authors, Licensee: John Wiley & Sons and Hindawi Publishing Corporation, under the Creative Commons Attribution License, copyright 2018.

antibody (trastuzumab or rituximab)-conjugated AuNPs (40 nm) by cancer cells *in vitro*. For this, SKBR3 and Raji lymphoma cancer cells with trastuzumab-AuNPs and rituximab-AuNPs, respectively after which the cells were collected in Eppendorf tubes which were fixed in a PMMA phantom holder. The study exploited the tendency of trastuzumab (Herceptin) to bind with HER2-positive breast cancer cells (SKBR3) and rituximab to bind to the CD20 antigen of B-cell lymphomas. The authors reported AuNP-trastuzumab uptake in SKBR3 cells and AuNP-rituximab uptake in Raji cells (Fig. 3C) as detected and imaged by MARS SPCCT. They demonstrated the potential application of SPCCT in molecular imaging, which allows the detection and quantification of functionalized AuNP uptake by cancer cells *in vitro*.[63,65]

Several reports confirm the size-dependent uptake of NPs by cancer cells. In this context, a study described higher uptake of 18 and 80 nm "as prepared" AuNPs in ovarian cancer cells (OVCAR5 and SKOV3), and selective targeting of ovarian cancer *in* an *in vivo* model using LHRH peptide-conjugated (PEG-peptide mixed monolayer) AuNPs.[66,67] Another study also showed the accumulation of 15 nm AuNPs at the periphery of Lewis lung carcinoma implanted in mice. These studies highlight the importance of SPCCT for the detection and quantification of AuNPs in cancerous cells and tissues both *in vitro* and *in vivo*.[65] In another study, AuNPs functionalized with an anti-plasma membrane heat-shock protein antibody were used for *in vitro* cell culture and *in vivo* imaging in mice. They showed that functionalized AuNPs accumulated in the plasma of tumor cells but not in normal cells. Spectral CT imaging and histological studies confirmed the selective accumulation of functionalized AuNPs in different tumor mouse models[64] (Fig. 4A).

One study used DECT to quantify the accumulation of iodine, bare AuNPs, and RGD peptide-functionalized AuNPs (25 nm) to enhance the radiation therapy tumor dose in mice. Human umbilical vein endothelial cells (HUVECs) were exposed to AuNPs in an *in vitro* experiment. Darkfield microscopy showed an increased accumulation of AuNPs in HUVECs, especially when labeled with the RGD peptide (Fig. 4B). They quantified the effect of AuNPs on radiation-induced tumor vascular disruption. DECT allowed for the measurement of AuNP accumulation and assessment of vascular permeability.[68] In yet another study, DECT was employed to measure the concentration of AuNPs functionalized with folic acid (FA-AuNP) in human nasopharyngeal cancer cells. NPs (15 nm in size) were synthesized, and different concentrations (0.25–2 mg mL^{-1}) were placed in the phantom for imaging at 80 and 140 kVp. KB cells incubated with FA-AuNPs under different concentrations were detected and quantified by DECT. The study reported that FA-AuNPs are suitable candidate for targeted DECT imaging of nasopharyngeal cancer cells.[69] In another study, Cormode *et al.* investigated SPCCT imaging of AuNPs functionalized with high-density lipoprotein (Au-HDL). The AuNP formulation was used for the characterization of macrophage burden, calcification, and atherosclerotic plaque in apo E-KO mice and in a phantom. SPCCT with a 3 mm-thick cadmium telluride detector was used to acquire images for six energy windows (0–25, 25–34, 34–51, 51–80, 80–91, and 91–110 keV).[70] Material decomposition (MD) using the maximum likelihood method

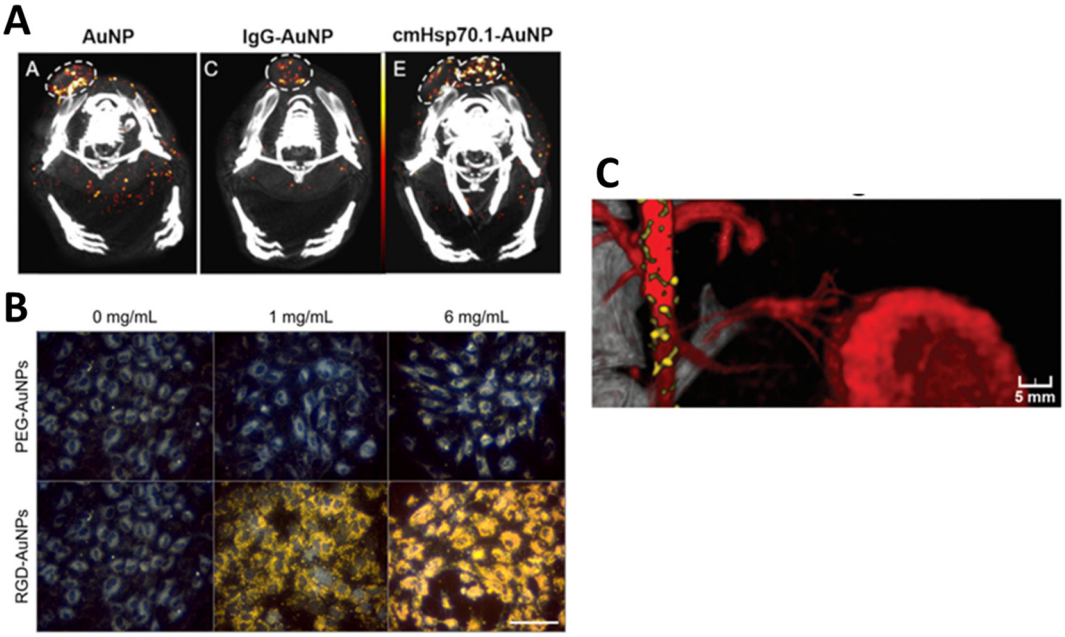

Fig. 4 Tumor detection in tumor-bearing mice using spectral photon-counting CT. Functionalized AuNPs were located in the tumor periphery and were highly dispersed in the tumor center (A), reproduced from ref. 64 with permission by the authors, Licensee: MDPI, Basel, Switzerland, under the Creative Commons Attribution License, copyright 2020. Darkfield microscopy showing PEG-AuNP and RGD-AuNP targeting of endothelial *in vitro* for 1 mg mL^{-1} and 6 mg mL^{-1} of gold (B), reproduced from ref. 68 with permission from Ivyspring International Publisher, copyright 2018, and SPCCT fused images of atherosclerotic rabbit aorta 2 days after injection of AuNPs and iodine (Iomeprol, 400 mg mL^{-1}) as contrast agents (C), reproduced from ref. 59 with permission from Radiological Society of North America, copyright 2021.

was used to detect gold and iodine. Phenomena such as photoelectric and Compton effects allowed the differentiation of Au-HDL, iodine, and calcium phosphate in the phantoms. During the *in vivo* study, accumulation of Au-HDL was detected in the aortas of atherosclerotic mice. This demonstrates that SPCCT imaging of Au-HDL can be used to detect macrophages in atherosclerosis.[70]

An *in vivo* study used PEG-conjugated AuNPs to quantify macrophage burden in atherosclerotic plaque after intravenous injection of 3.5 mL kg^{-1} AuNP-PEG (stock −65 mg mL^{-1}) in a rabbit model. AuNP-PEG K-edge imaging allowed plaque image enhancement. The results were confirmed by histological examination, transmission electron microscopy, inductively coupled plasma analysis, and optical emission spectrometry. Fig. 4C shows the SPCCT image of the rabbit aorta where AuNPs (yellow) accumulated in the plaque and iodine as an additional contrast agent (red). This illustrated the ability of SPCCT to image AuNP accumulation in atherosclerotic plaques. Detection and quantification of the Au concentration in the macrophage burden in atherosclerotic plaques are possible with SPCCT.[59] Si-Mohamed has also employed the PEGylated-AuNPs in conjunction with SPCCT to investigate the biodistribution of gold (a high-*Z* material) as well as molecular imaging of mononuclear phagocyte system (MPS) in a rabbit model.[71] Another study reported the use of SPCCT to visualize Au-labeled macrophages extracted from the bone marrow and implanted these cells as therapeutic cells in 21 rats with brain damage. This study showed the feasibility of using AuNP-labeled macrophages for two weeks after implantation in clinically stimulated brain injury. This shows that unlike the short-lived positron emitters used in PET imaging, AuNPs can be imaged for a much longer period using SPCCT.[72] Wan *et al.* used silica coated AuNPs further functionalized with DNA Transfectin 3000 as a potential cellular probe for tracking stem cells in bone regeneration using DECT. The study suggested that DECT imaging with AuNPs–SiO_2 allowed accurate and noninvasive tracking of stem cells in an *in vivo* model. This study was scoped for the potential new possibilities of stem cell-mediated bone regeneration. Additionally, gold nanoparticles were found to be minimally toxic and did not adversely affect stem cells or surrounding tissues.[73]

Cormode *et al.* used a spectral CT to investigate the feasibility of simultaneously imaging and quantifying PEG-coated AuNPs and iodine contrast agents in a phantom and *in vivo* in New Zealand white rabbits. They concluded that SPCCT allows the simultaneous imaging and quantification of AuNPs and iodine as contrast agents *in vivo*.[74] Si Mohamed *et al.* used Au, gadolinium, and iodine-based contrast agents at concentrations that yielded the same HU of 280. Contrary to conventional CT, they showed that SPCCT allowed differentiation between contrast agents in a phantom study using material recognition methods.[25] Dong *et al.* studied the effect of the size (4–152 nm) of AuNPs capped with 5 kDa m-PEG as an image contrast agent using two conventional clinical CT scanners, two micro-CTs, and an SPCCT. They reported that at the same concentrations (0–10 mg mL^{-1}) in a phantom, there was no significant difference in image contrast owing to size variability. However, the HU values increased linearly with concentration for all sizes. In addition, the study concluded that 15 nm or smaller AuNP-mPEG had a longer circulation time in six mice injected with an NPs dose of 500 mg kg^{-1}. Larger NPs accumulate in the liver and spleen.[75] Zambrano-Rodrigues *et al.* used dual energy micro-CT to image AuNPs and iodine as contrast agents to enhance the myelogram in the rat (sample size −18). They used commercially available iodine-based (Iomeron® 400 and Fenestra® VC) and AuNP-based (AuroVist™ 15 nm, Nanoprobes) contrast agents. They obtained a better contrast-to-noise ratio (CNR) using single-energy time subtraction with Iomeron as a contrast agent. However, this study also showed the potential application of AuNPs as contrast agents to obtain high-resolution myelograms with micro-CT.[76]

Sadeghian *et al.* conducted an MC simulation study to simulate the SPCCT imaging of gold, silver, and bismuth 50 nm NP and iodine at concentrations of 2, 4, and 8 mg mL^{-1} in a water-filled cylindrical phantom. The simulation indicated that high-*Z* NPs had a higher CNR than iodine.[77] Jo *et al.* used the Monte Carlo method to simulate SPCCT imaging and DECT for three-material decomposition (lipid, iodine, and gold nanoparticles) to identify vulnerable plaques in the coronary artery. The proposed technique analyzes the composition of plaques by quantifying the number of lipids and calcification. They modeled a coronary artery (3 mm diameter tube) filled with iodine contrast, AuNPs, or lipids. They found that the technique had good sensitivity and specificity for identifying the three materials. This study suggests that this new technique has the potential to detect the accumulation of AuNPs in plaques in the presence of lipid and iodine contrasts in the lumen. This has the potential clinical application to improve the diagnosis and management of coronary artery disease.[78] Table 1 captures a summary of AuNP studies performed since 2014 with a focus on the size and shape of the nanoparticles, nanoparticle size, targeting agent, the type of study (in phantom, *in vitro*, *in vivo*, or simulation), and the application.

4. Gadolinium (64) nanoparticles

Gd is a high-*Z* ($Z = 64$) metal with a high X-ray attenuation coefficient; therefore, Gd- or Gd-based compounds (contrast agents, GBCA) have been extensively explored as contrast agents in *in vitro*, *in vivo*, and clinical settings, using traditional and emerging imaging modalities. A recent study explored GBCA and iodine as contrast agents for SPCCT imaging to enhance high spatial resolution in an *in vivo* model. The analysis suggested better diagnostic quality images using SPCCT compared with CT ($p < 0.0001$) and SPCCT contrast material maps illustrated the visual differentiation of both contrast agents. The study also reported clear differentiative images of the peritoneal cavity and abdominal organs in rat model with potential application for the detection of peritoneal metastases.[80] Despite their extensive use, these contrast agents

Table 1 AuNP studies in DECT and SPCCT since the last review 2014[24]

NP (size (nm))	Functionalization	Study type	Application	Ref.
Au (3.1)	HDL	In phantom and in mice aorta	Detect macrophages in atherosclerosis	70
Au (12.5)	PEG coating	In phantom and New Zealand rabbits with atherosclerotic plaque	Quantify macrophage burden in atherosclerotic plaque	59
Au (50), Ag (50), Bi (50)	None	In phantom	Monte Carlo simulation to measure contrast	79
Au (45 ± 15)	Anti-plasm membrane heat shock protein antibody	*In vitro* cell culture and in mice	Functionalized AuNP targeting of cancer cells	64
Au (22)	11-Mercaptoundecanoic acid	In phantom, in cell culture	AuNP used to label implanted microphages in damaged rat brain	72
Au (15)	Folic acid	Cell culture	Au–FA targeted nasopharyngeal cancer cells	69
Au (4–152)	m-PEG	In phantom and in mice aorta	Contrast depends on concentration does not size of NP	75
Au (18)	None	In phantom	Color imaging of Au, Gd, and iodine when they give the same HU.	25
Au (18, 40, 60, 80)	None	In phantom, in cell culture, and in mice	*In vitro* and *in vivo* targeting and imaging of cancer cells	65
Au (40)	Herceptin	In phantom, in cell culture	*In vitro* and *in vivo* imaging of cancer cells	63
Au (25)	RGD peptide	In cell culture and in mice	Targeting of endothelial cells and assessment of vascular permeability	68
Au (12)	PEG	In phantom and *in vivo* rabbits	Quantification of AuNP and iodine contrast agents *in vivo*	74
Au (12.5)	PEG	*In vivo*	Quantification and biodistribution of NPs *in vivo*	71
Au (20)	Silica and DNA transferrin 3000	*In vitro* and *in vivo* rabbits	*In vitro* and *in vivo* targeting bone marrow stem cells using AuNP–SiO_2 with DNA transferrin 3000	73

cause side effects due to the release of free Gd^{3+} ions from the chelated group which then accumulate in major organs such as the kidney, brain, and bone; and are linked to causing nephrogenic systemic fibrosis.[81,82] Therefore, this necessitates urgency to design systems that can chelate and stabilize the Gd^{3+} ions while harnessing the potential of Gd as a contrast agent. This can be achieved by developing Gb-based nanoparticulate formulations as an effective contrast agent with improved biocompatibility. GdNPs acquire the same properties; thus, NPs have been investigated as image contrast enhancers for EI and SPCCT imaging. The use of GdNPs in spectral CT imaging allows for differentiation between tissue types based on NPs uptake variability or elemental composition. This can aid in the diagnosis of certain diseases such as cancer. Hence, the use of gadolinium nanoparticles in DECT and SPCCT imaging offers a great opportunity to improve the accuracy of diagnostic imaging and to assist in the early detection of disease. These nanoparticles are biocompatible and can be easily synthesized in the size range of 10–100 nm, permitting longer systemic circulation. Additionally, by conjugating these nanoparticles with targeting molecules such as antibodies, site-specific targeting is possible. These NPs have been frequently used to enhance contrast in MRI, which makes GdNPs a potential dual-modality contrast agent for X-ray and MRI imaging.[83]

Kochebina *et al.* used SPCCT and SPECT to image and quantify GdNPs in phantom studies. GdNPs were labeled with gamma-emitting[84] In for SPECT imaging using a Philips Healthcare System. A prototype with maximum likelihood material decomposition methods with 0.25 mm spatial resolution in all directions was used. The study concluded that GdNP detection and quantification are possible with SPCCT and SPECT; however, SPCCT does not require radiolabeling while preserving the sample scan time compared to SPECT.[85] A study by Badea *et al.* systematically investigated the preclinical efficacy of Gd and iodine-based liposomal nanostructures as contrast agents for cancer imaging. They also imaged mice administered with liposomal iodine (145 nm size and 0.2 g Gd kg^{-1}) and liposomal GdNPs (270 nm, 0.2 g Gd kg^{-1}). They demonstrated that DECT allows simultaneous qualitative and quantitative analysis of iodine and Gd-based contrast agents. To satisfy the dose limit of detectability and to keep the signal-to-noise ratio (CNR) at a minimum, the minimum threshold concentration of the contrast agent had to be 2.46 mg mL^{-1}.[86]

5. Bismuth (83) nanoparticles

Among several high-*Z* elements, bismuth (Bi)-based salts and nanostructures (NSs) have been developed and used for targeting and imaging different diseases using SPCCT imaging. One such formulation includes phospholipid nanostructures with a core containing a high density of bismuth-*n*-decanoate. The formed nanostructures were in the size range of 180–250 nm and displayed a surface charge between −20 mV and −27 mV. This system was termed as 'NanoK' where the nanostructures were modified with biotin to mediate avidin-biotin interaction for binding the nanostructures to the fibrin clot.[23] The *in vitro* results demonstrated a significant enrichment of the signal relative to non-metallic nanoparticles. An atherosclerotic rabbit was used for the *in vivo* pilot study, and a balloon-overstretched injury-induced thrombus was formed in the iliac artery. The rabbit was treated with fibrin targeted NanoK, and spectral CT confirmed clear differentiation between the intravascular lesion and skeletal anatomy of the animal. The study also assessed the bioelimination and tissue impact of the heavy

metal containing NanoK formulation in an adult Balb/C mouse model. The results indicated the presence of less than 10 ppb mL^{-1} of bismuth in the liver, spleen, and kidney, which is considered below the detection limit of the instrument. The study also determined tissue functionality after nanoparticle treatment in a mouse model and reported that both liver and renal functions were within normal limits.[23]

Another study used dopamine (DA)-and hyaluronic acid (HA)-functionalized bismuth fluoride (BiF_3) NPs (BiF_3@PDA@HA) to accurately diagnose liver fibrosis using spectral CT.[87] By modifying nanostructures with HA, cell-specific targeting of hepatic satellite cells is possible, which is a hallmark of liver fibrosis. *In vitro* studies confirmed faster cellular uptake of the HA-coated nanoparticles compared to PEG-modified systems (BiF_3@PDA@PEG) used as a non-specific control. The *in vivo* assessment further validated the *in vitro* observations using the two formulations (HA *versus* PEG-modified systems) in a mouse model. The spectral CT results demonstrated significant enrichment of Bi for the targeted BiF_3@PDA@HA group in the diseased liver tissue up to 80 min post-injection. On the other hand, the non-target group (BiF_3@PDA@PEG) showed no signal enhancement in the hepatic parenchyma. Additionally, the targeted nanoformulation showed no contrast enhancement in the healthy liver, suggesting the potential utilization of this system for resolving diseased tissue from healthy liver tissue. Fig. 5(A–H) represents the SEM images of BiF_3@PDA@HA nanoparticles along with the chemical analysis using FTIR, followed by a comparative image from traditional CT and spectral CT of the liver (and surrounding organs), pre-and post NPs injection, and an increase in intensity with time in the targeted group. The image also shows the energy-dependent attenuation of the targeted region after BiF_3@PDA@HA NPs injection in the *in vivo* model, and changes in the spectral house units (HU) of the liver and tissue at different

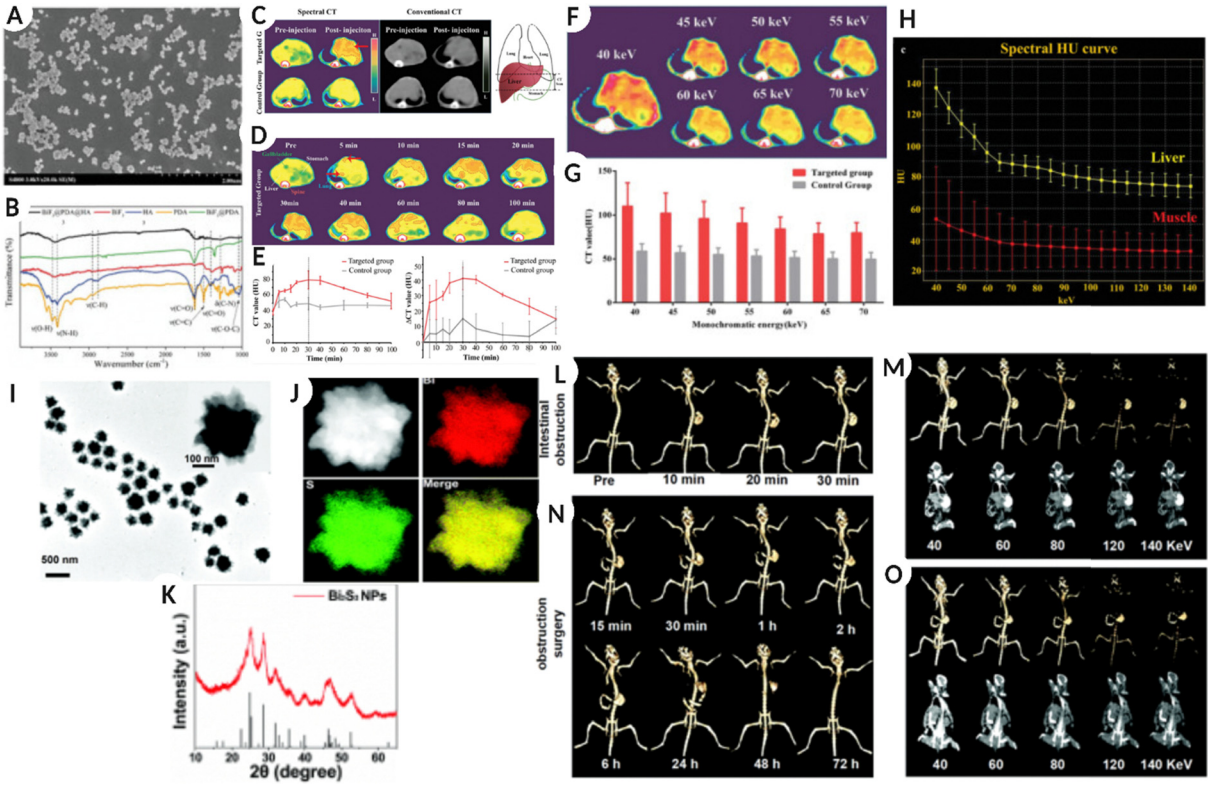

Fig. 5 (A) Scanning electron microscopy (SEM) images of BiF_3@PDA@HA. (B) Fourier transformation infrared spectra (FT-IR) of BiF_3@PDA@HA, BiF_3@PDA, BiF_3, HA, and PDA. (C) Representative CT images were acquired at two-time points (pre-injection and 30 min after the injection of BiF_3@PDA@HA) for two groups *via* spectral CT (70 keV) and conventional CT (140 kVp). (D) Representative spectral CT images of the targeted group before and after the injection of BiF_3@PDA@HA. (E) Dynamic time courses of CT value and CT value change (ΔCT value) of hepatic parenchyma of the targeted group (red line, n = 3) and control group (grey line, n = 3). (F) 40–70 keV monochromatic images of the targeted group. (G) Comparison between the targeted group (n = 3) and the control group (n = 3) in CT value of monochromatic images of 40–70 keV. Data were presented as mean ± standard deviation. (H) Spectral HU curves of the liver (yellow line) and muscle (red line) of the targeted group. (A–H: Reproduced from ref. 87 with permission from Wiley-VCH GmbH, copyright 2021.) (I) TEM images of Bi_2S_3 NPs. (J) HAADF-STEM images of Bi_2S_3 NPs and the EDX elemental mapping of Bi and S elements and the merged image. (K) XRD pattern of Bi_2S_3 NPs and the standard Bi2S3. (L) Traditional CT imaging of the mouse model with intestinal obstruction after oral administration of 400 μL Bi2S3 NPs (26 mg mL^{-1} Bi_2S_3 NPs) at 120 kV. (M) Spectral CT imaging of the mouse model with intestinal obstruction at 30 min after oral administration of 400 μL Bi2S3 NPs (26 mg mL^{-1} Bi2S3 NPs) at various X-ray energies (40, 60, 80, 120, and 140 keV). (N) Traditional CT imaging of the mouse model with intestinal obstruction after surgery to relieve intestinal obstruction at 120 kV. (O) Spectral CT imaging of the mouse with surgery to relieve intestinal obstruction at 6 h under various X-ray energies (40, 60, 80, 120, and 140 keV) (I–O: Reproduced from ref. 6 with permission from Royal Society of Chemistry, copyright 2022). Image assembled with **https://BioRender.com**.

energy attenuations. Furthermore, because of the energy-dependent attenuation of Bi, the diseased area could be suitable for selecting different monochromatic energies *via* spectral CT.[87]

In a simulation-based study comparing the spectral properties of Au, Ag, and Bi NPs with an average diameter of 50 nm, the AuNPs generated the highest CT and CNR values. AgNPs demonstrated better performance at 80 keV, whereas a higher energy of 120 keV was required for BiNPs to generate a high CNR. These results suggest that NP-based contrast agents are superior to iodine with a higher CT number and CNR.[77] While another study suggested that iron oxide NPs coated with Bi (Fe_3O_4@Bi) or Au (Fe_3O_4@Au) produced the same image quality but better quality images were obtained between 100–120 keV for Bi-coated NPs.[88] Furthermore, bismuth sulfide (Bi_2S_3, 276 nm size) flower-like nanostructures or nanoparticles synthesized by a green strategy (highly monodispersed) showed high biocompatibility and absorption in the NIR range and excellent spectral CT imaging capability. The administered formulation generated accurate spectral CT images for the gastrointestinal tract as well as assisted with the diagnosis of intestinal obstruction as a result of growing tumor *in vivo*, as shown in Fig. 5(I–O).[6] Fig. 5I–K show the TEM image of Bi_2S_3 NPs, HAADF-STEM images with EDX elemental mapping of Bi and S elements, and XRD analysis of Bi_2S_3 NPs, respectively. Fig. 5L shows a traditional CT image of a mouse model with intestinal obstruction after oral ingestion of 400 μL Bi2S3 NPs (26 mg mL^{-1} Bi2S3 NPs) at 120 kV. Fig. 5M shows an SPCCT image of an *in vivo* model with intestinal obstruction after 30 min of oral administration of Bi2S3 NPs (400 μL, 26 mg mL^{-1} Bi2S3 NPs) at different X-ray energies (40, 60, 80, 120, and 140 keV). Fig. 5N is a traditional CT image of a mouse with intestinal obstruction after surgery, confirming relief from intestinal obstruction at 120 kV; Fig. 5O represents an SPCCT image of the same after 6 h under various X-ray energies (40, 60, 80, 120, and 140 keV).

6. Ytterbium (70) nanoparticles

Ytterbium (Yb), prior to consideration in nanoform, the chelated Yb form was reported for its application as a CT blood pool contrast agent with an optimal safety profile in the *in vivo* models.[89,90] Yb-based nanostructures have been extensively used as contrast agents in X-ray CT imaging.[91,92] However, their application in spectral CT imaging is gaining increasing momentum. The nano-colloidal suspension of Yb(III) 2,4- pentanedionate and phospholipids (egg phosphatidylcholine and dipalmitoyl phosphatidylethanolamine caproyl biotin) synthesized *via* self-assembly resulted in NPs with an average diameter of 150 nm. The nanoformulation was used for SPCCT to image non-occlusive microthrombi linked to ruptured plaques in patients with potential cardiac etiology. The results demonstrated excellent contrast both *in vitro* and *in vivo*, along with clearance of NPs *via* the RES route and bioelimination within a week of intravenous administration (Fig. 6A–I).[93] Fig. 6A shows the composition of Yb-based NPs, while the TEM, hydrodynamic diameter, AFM scan of particles on a glass slide, and physicochemical properties are shown in Fig. 6B–E. Fig. 6F shows a blood pool image using pseudo-conventional CT from the spectral measurement of the heart for a non-targeted Yb colloid injected in an *in vivo* model. Meanwhile, Fig. 6G and H are the reconstructed images after 1 and 20 iterations of the same, respectively. Fig. 6I is a volume-rendered CT image superimposed with the Yb signal (green dot/arrow), confirming the accumulation of targeted Yb nano colloid in the heart.

Some advantages of Yb-based NSs are the high abundance of Yb, lower toxicity when encapsulated within an appropriate carrier, and K-edge energy (61 keV) within the X-ray spectrum range recommended for clinical CT.[95–97] In one study, oleic acid, and DSPE-PEG 200 stabilized YbNPs were intravenously administered (1.0 mL, 70 mg mL^{-1} Yb) in rats as contrast agents. The YbNP formulation remained in the systemic circulation for longer with minimal toxicity and showed high efficacy compared to the iodine-based suspension for enhanced vascular imaging and disease diagnosis.[91] Another comparative study demonstrated higher contrast generation by YbNPs relative to traditional AuNPs for hydrogel labelling thus permitting its localization and tracking *in vivo* for different biomedical applications (Fig. 6J–N).[94] Fig. 6J shows a 2D CT image of the coronal view of a mouse model before and after YbNP-hydrogel (blue) and AuNP-hydrogel (yellow) administration for five minutes and 1 week, respectively. Fig. 6K shows the total CT attenuation-based quantification of Yb and Au at the same time points. Fig. 6L shows a 3D reconstruction of the YbNP hydrogel based on the information collected in Fig. 6J. Fig. 6M shows a 3D volume-rendered CT image of an *in vivo* model injected with the YbNP hydrogel (blue) and AuNP hydrogel (yellow) at different times. Fig. 6N shows the biodistribution of Yb and Au in the major organs, tissues, and carcasses at the end of the study after 2 weeks. By successfully modifying YbNPs with SiO_2 and *N*-nitrilotriacetic acid (NTA), preferential calcium chelation was possible, which allowed specific targeting of the damaged bone. The crack-targeted Yb NPs successfully generated a high-contrast spectral CT image of the damaged tissue in real time and differentiated healthy and cracked bone tissue *in vivo*.[98]

Ytterbium is also known for its up-conversion luminescence, which makes Yb NSs suitable for multimodal imaging platforms. To harness the multi/bimodal capability of Yb, PEGylated $NaYbF_4$:Tm^{3+} NPs (UCM, average size 20 nm) were used for SPCCT and NIR-fluorescence imaging. This allowed the generation of high contrast for SPCCT and strong NIR-fluorescent emission both *in vitro* and *in vivo*. The UCM NPs formulation showed 75% more CT contrast efficacy than clinically available iobitridol.[99] Additionally, the nanoparticles were non-toxic to HL-7702 and RAW264.7 cells up to 1.6 mg Yb mL^{-1}, while at 150 mg Yb kg^{-1} concentration in the *in vivo* model. The administered formulation showed low or no tissue damage and was removed from the systemic circulation *via* feces and urine within 7 days, with some accumulation in the spleen 1 month post-injection. In another study, silica- and PEG-stabilized hybrid Yb and barium NPs ($BaYbF_5$@SiO_2@PEG) significantly enhanced the image contrast

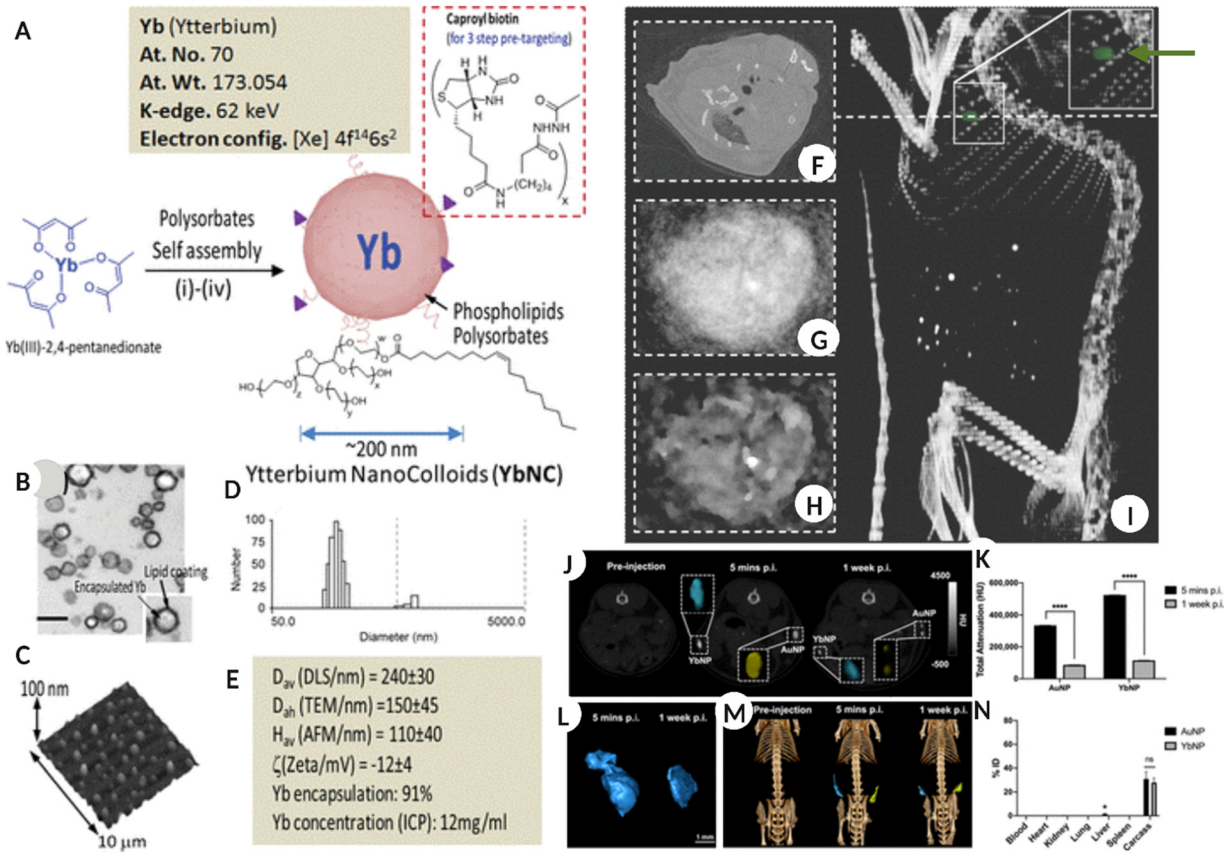

Fig. 6 (A) Schematic representation for the synthesis of Yb nano-colloids along with elemental information. (B) TEM image of Yb nanocolloid encapsulated in lipid NS. (C–E) AFM image of Yb nanocolloid dried on a glass slide, the number size distribution of colloid and different physicochemical properties of the same. (F) blood pool imaging using pseudo-conventional CT from the spectral measurement of the heart for non-targeted control *in vivo* model administered with Yb nanocolloid. (G and H) image reconstruction after 1 and 20 iterations of the same, respectively. (I) volume rendered CT image super-imposed with Yb signal (green dot/arrow) showing accumulation of targeted Yb nanocolloid in the heart. (A–I: Reproduced from ref. 93 with permission from American Chemical Society, copyright 2012.) (J) A 2D CT image of the mouse in coronal view, pre and post-YbNPs-hydrogel – blue color and AuNPs-hydrogel – yellow color injection after 5 min and 1 week. (K) total CT attenuation-based quantification of Yb and Au after 5 min and 1 week. (L) representing the 3D reconstruction of YbNPs-hydrogel based on data in (J). (M) Representative 3D volume rendered CT image of *in vivo* model introduced with Yb-blue and Au-yellow based hydrogels at different times. (N) information on biodistribution of Yb and Au in major organs and tissues and carcass administered with NPs hydrogels after 2 weeks. (J–N: Reproduced from ref. 94 with permission from American Chemical Society, copyright 2022.) Image assembled with **https://BioRender.com**.

with improved circulation time compared to clinical iodine-based contrast agents. The improved circulation time was attributed to the antifouling capability of PEG, suggesting the potential use of this nanoformulation as a blood pool CT contrast agent for diagnosing diseases such as myocardial infarction and thrombosis. This study validated the efficacy of the formulation for high-resolution blood pool imaging in both small (rat model) and large (rabbit) animal models with clear contrast enhancement within 2 h of administration.[100] The long-term toxicity of the administered formulation was determined by histology, which showed no noticeable signs of tissue damage and/or inflammation.

7. Hafnium/hafnia (72) nanoparticles

Another element that has been investigated to some extent is Hafnium (Hf) which has a K-edge of 65 keV that lies between those of gadolinium (50 keV) and gold (80 keV). In a recent *in vitro* study, fucoidan-modified HfO_2 NPs were used for early diagnosis of atherothrombosis by exploiting the affinity of fucoidan for P-selectin, a glycoprotein biomarker for this pathological condition. The specific targeting of functionalized NPs to the target cell type along with good biocompatibility and better X-ray attenuation when compared to unmodified and citrate-modified counterparts, suggests a great potential of the designed formulation as an X-ray contrast agent for diagnosing atherothrombosis.[101] While in another study ultra-small (5 nm) HfO_2 NPs were employed to assess bone microdamage, which is traditionally evaluated using invasive histomorphometry (Fig. 7A–J).[61] The study utilized ligand modified HfO_2 NPs, which accumulated at the microdamage site, and the generated signals differentiated the accumulated nanoparticles, bone, and soft tissue. Additionally, *in vivo* assessment confirmed that HfO_2 NPs were removed *via* the RES system and did not induce any adverse toxic responses, as validated by histological analysis.[61] Fig. 7A–D show the physicochemical properties of

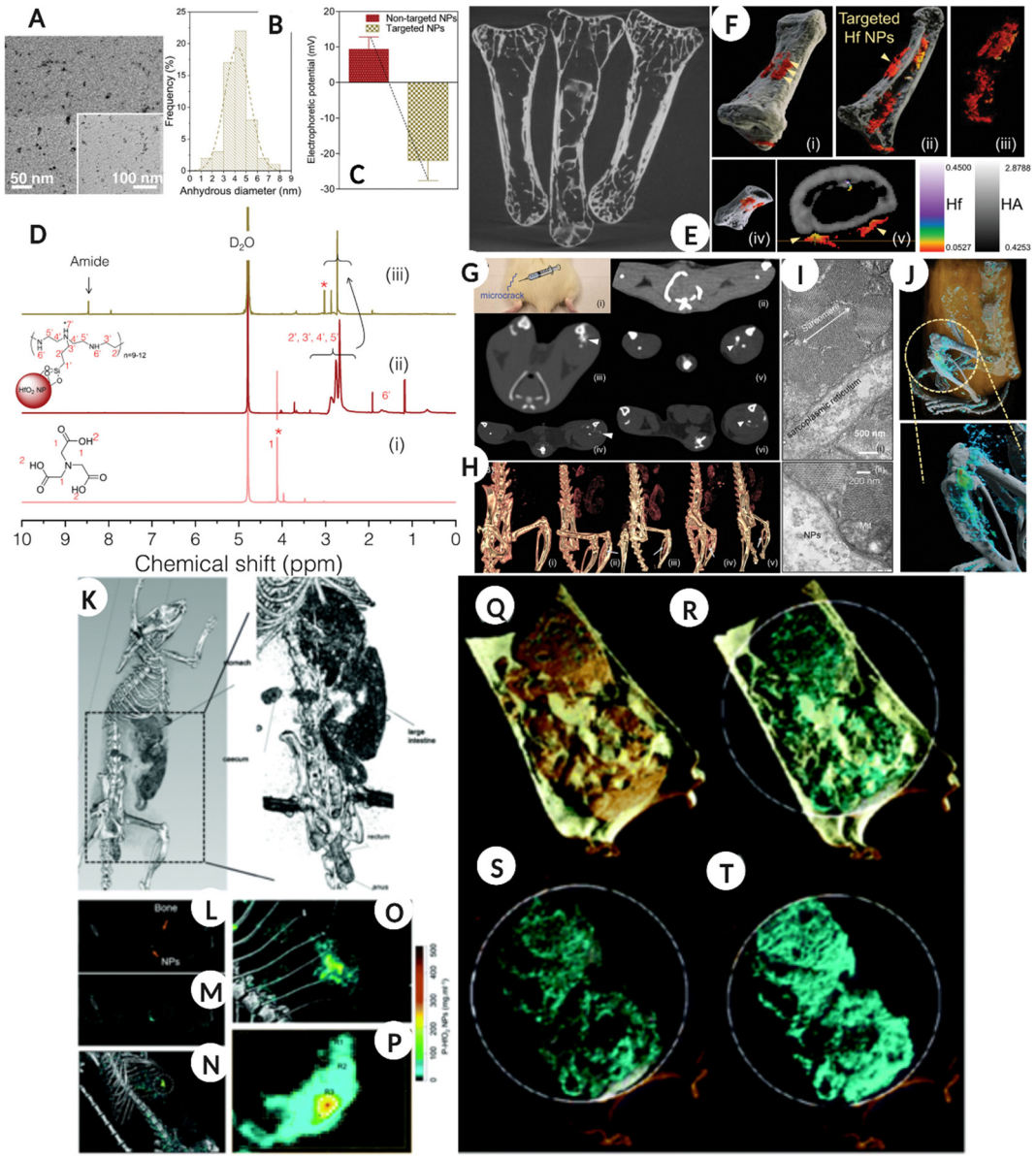

Fig. 7 Bone microdamage detection (A–J). (A–D) TEM image of targeted hafnia NPs, hydrodynamic diameter by frequency distribution along with surface zeta potential before and after immobilization of targeting molecule and ^{1}H NMR spectra of NTA 'i', 'as prepared' 'ii' and surface modified 'iii' Hf NPs. (E) Showing the micro-CT image of bones clean, soaked in targeted Hf solution, and soaked in 'as prepared' Hf NPs solution. (F) (i–v) show spectral CT 3D images of *ex vivo* human bone microdamage and distribution of targeted Hf NPs (red color) and bone (white/gray) with the color scale. The arrow shows the location of the microdamage. (G) The bone microdamage was investigated using traditional CT in an *in vivo* model (control sham-operated model-ii, 'as prepared' NPs 30 min-iii, 'as prepared' NPs 5 h-iv, and targeted Hf NPs after 30 min and 5 h-v and vi respectively). (H) The 3D reconstructed spectral CT image of G, the arrow represents Hf NPs accumulation (i – control, ii – nontargeted NPs 30 min, iii – nontargeted NPs 5 h, iv – targeted NPs 30 min, v – targeted NPs 5 h). (I) TEM image of injection site showing no NPs aggregation and accumulation. (J) *in vivo* bone microdamage evaluation and Hf NPs differentiation from bone and surrounding tissue using spectral CT, gray is bone, cyan-green is a high concentration of Hf NPs, blue is low concentration and white is calcium. (A–J: Reproduced from ref. 61 with permission from Wiley-VCH Verlag GmbH & Co. KGaA, Weinheim, copyright 2019). Gastrointestinal tract imaging using hafnium oxide NPs (K–T). (K) A conventional CT of a rat model fed with HfO2 NPs, showing the accumulation of NPs in the abdominal region. (L) Coronal view of one energy bin showing NPs and bone. (M) is the coronal view for hafnia channel overlay with energy bin while N is a 3D volumetric reconstruction of material decomposition differentiating bone and HfO2 NPs. (O & P) are the magnified images of the bright green region in image (N). (Q–T) are the material weight spectral photon-counting images of the GI tract where the rat was fed with an HfO_2 capsule. (Q) Yellow color represents lipid, cyan is for HfO_2 NPs, (R) cyan – HfO2 NPs and gray – hydroxyapatite, (S & T) cyan – HfO_2 NPs. (K–T: Reproduced from ref. 102 with permission from Royal Society of Chemistry, copyright 2022.) Image assembled with **https://BioRender.com**.

Hf NPs, such as TEM, hydrodynamic diameter, surface zeta potential, and NMR, for the as-prepared and surface-modified NPs. Fig. 7E represents the bone sample images for "not exposed," exposed to targeted, and 'as prepared' HfNPs suspension collected using micro-CT. In addition, Fig. 7F(i–v) shows the 3D spectral CT images of *ex vivo* human bone microdamage

and the targeted Hf NPs distribution (red color) and bone (white/gray) with a color scale, highlighting the location of microdamage. Fig. 7G represents the bone micro-defect imaged using conventional CT in an *in vivo* model (control sham-operated model-ii, 'as prepared' NPs 30 min-iii, 'as prepared' NPs 5 h-iv, and targeted Hf NPs after 30 min and 5 h-v and vi respectively). While Fig. 7H is a 3D reconstructed spectral CT image of 7G, the arrow represents Hf NPs accumulation (i – control, ii – non-targeted NPs 30 min, iii – nontargeted NPs 5 h, iv – targeted NPs 30 min, and v – targeted NPs 5 h). Fig. 7I and J show the TEM image of the injection site, confirming no aggregation and accumulation of Hf NPs and bone microdamage evaluation and Hf NPs differentiation from bone and surrounding tissue using spectral CT for the *in vivo* model.

In a recent study, ultra-small 1–2 nm HfO_2 NPs were designed for oral ingestion and hitchhiking probiotic bacterial cells for spectral CT imaging of the gastrointestinal (GI) tract. The nano–bio interaction for engineered NPs delivery combines natural delivery with harnessing probiotic cell functions. The nano–bio-hybrid formulation was prepared by the passive uptake of HfO_2 by probiotic bacteria, including *E. coli* and *L. lactis*, following which the bacteria were freeze-dried and could be effectively revived post-processing. The idea behind this was that the modified probiotic can be effectively packed in an oral formulation, such as a capsule, to be administered to the patient. As a proof of concept, the authors prepared bio-HfO_2 by incubating *E. coli* with 54 mg of NPs for 4 h after which the bacteria were washed, freeze-dried, and resuspended in PBS for imaging using spectral CT. The imaging results confirmed that bio-HfO_2 could generate a high-contrast colored image of the GI tract, intestine, cecum, and small bowel diverticula within 30 min of oral ingestion. The results confirmed that the nanoparticle system was protected from degradation under harsh GI conditions and systemic absorption, thus offering a platform that can be used for GI imaging (Fig. 7K–T).[102] Fig. 7K is a traditional clinically available CT image of a rat model fed with HfO_2 and a high-resolution image showing the accumulation of NPs in the abdominal region. Fig. 7L shows the coronal view of one energy bin showing NPs and bone, and Fig. 7M shows the coronal view of the hafnia channel overlay with an energy bin. In addition, Fig. 7N shows a 3D volumetric reconstruction of the MD analysis with clearly distinguishing bone and HfO_2 NPs. Fig. 7O and P are magnified images of the bright green region in Fig. 7N. Fig. 7Q–T are the SPCCT images of the GI tract where rats were fed with HfO_2 capsule where lipid is represented by a yellow color, HfO2 NPs are shown by cyan, and HA by gray color.

Another study utilized the ability of Hf to excite surface phonon polariton nodes in the mid-infrared region, which is like surface plasmons for metal NPs such as Au and Ag. This study highlights yet another application of HfO_2 NPs (7–31 nm size range), which can potentially be used for photonic biosensing applications as well as contrast agents for MARS spectral CT applications.[103] The literature has also proposed the potential use of PVP-stabilized Hf NPs (10–20 nm) to target human tumor xenograft murine models and differentiate the tumor and its vasculature system. Furthermore, the surfaces of these three NP types were conjugated with antibodies using CLICK chemistry, which successfully targeted the cdl33(+) SKOV3-IP cells both *in vitro* and *in vivo*, which are primarily responsible for the metastasis and poor prognosis of ovarian cancer.[83,104]

8. Tantalum (73) nanoparticles

Tantalum (Ta) has a K-edge energy of 67.3 keV close to the mean photon energy region of X-ray spectra typically used in SPCCT imaging. Ta also has properties such as high elemental density (16.4 g cm^{-3}), affordability, biocompatibility, and excellent physicochemical properties, making it suitable for contrast agent applications.[105] In general tantalum oxide (Ta_2O_5) is water-insoluble; however, after modification with (2-diethyl phosphate ethyl) triethoxy silane, 3-(trimethoxysilyl) propyl-*N*,*N*,*N*-trimethylammonium chloride, or 2-(carbomethoxy)-ethyl trimethoxy silane, the NPs remained in suspension for months and were injectable.[106,107] In addition, in comparison with clinical iodine as a contrast agent, the Ta_2O_5 NPs produced a higher image contrast in *the in vivo* model.[106] In a similar study, fluorescently labeled PEG-silane-conjugated TaO_x NPs (PEG-RITC-TaO_x) were synthesized to permit simultaneous imaging *via* fluorescence and *in vivo* X-ray CT imaging. The administered NPs remained in the systemic circulation for longer durations (around 3 h) with bright high-contrast images while demonstrating little toxicity (two weeks post NP administration) (Fig. 8).[108] Fig. 8A–C shows the TEM image of tantalum NPs, 'as prepared,' and PEG-RITC, followed by the absorbance-fluorescence spectra for free RITC and colloidal PEG-RITC-TaO_x. Fig. 8D shows the H & E-stained tissue samples from organs (top-bottom: liver, spleen, heart, kidney, and lung) at different time points (control, days 1, 3, 7, and 15), confirming minor toxicity in the liver. Fig. 8E shows a 3D volumetric rendered image of the *in vivo* model using spectral CT (top-ventral and bottom-lateral sides of the heart and great vessels) after NPs injection. Fig. 8F, top row represents the heart and liver coronal view along the dotted line in Fig. 8E, while the bottom row shows organs such as the spleen, kidney, and inferior vena cava for the same. Fig. 8G shows sentinel lymph node mapping and resection in the *in vivo* model using SPCCT volumetric rendering after 2 h of intradermal NPs injection.

The precise location of the sentinel lymph node is critical for determining tumor metastasis and can be useful in avoiding unnecessary tissue removal during surgery. By carefully mapping the lymph nodes, this can be avoided, and the study demonstrated that by intradermal administration of PEG-RITC-TaO_x, the lymph node location could be monitored. This was feasible due to the enhanced X-ray contrast, following which the tissue could be removed using fluorescence imaging. The results presented in this study confirmed the presence of NPs in excised tissue, but no histological changes were observed.

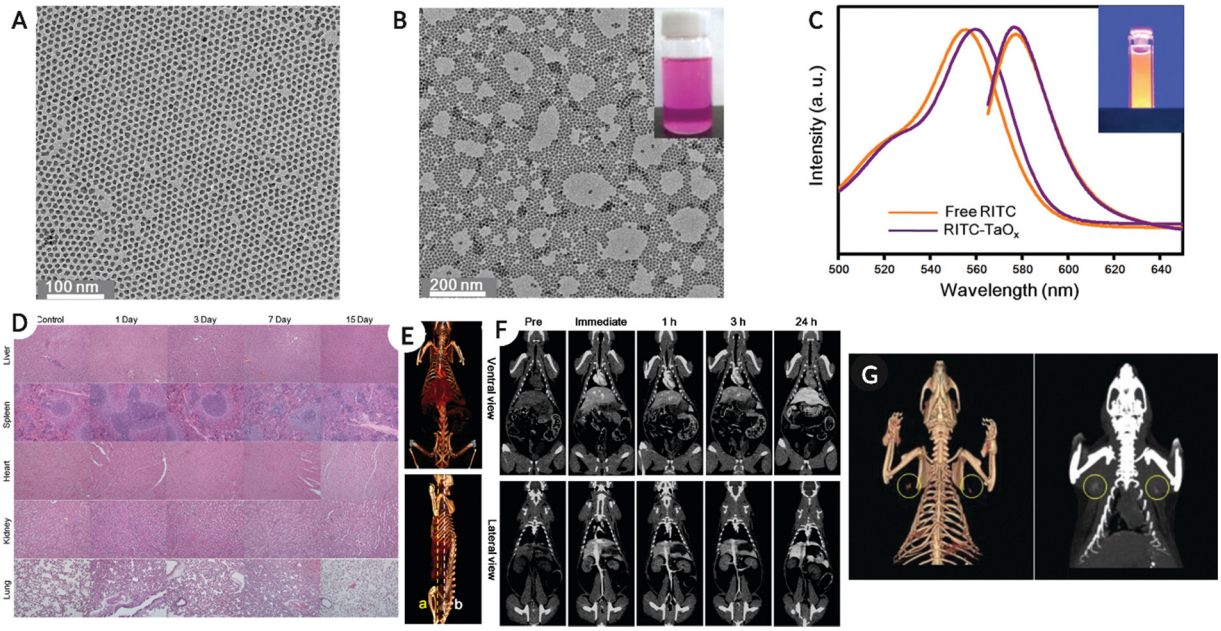

Fig. 8 (A–(C) Physico-chemical characterization of tantalum NPs, showing TEM images for 'as prepared', PEG-RITC modified NPs and absorbance-fluorescence spectra for free RITC and PEG-RITC-TaO_x colloid. (D) H & E-stained tissue samples from organs (top-bottom: liver, spleen, heart, kidney, and lung) at different time points (control, day 1, 3, 7 and 15) showing minor toxicity of NPs (injected with 1 mL of NPs colloid in the tail vein at 840 mg kg^{-1} concentration) in the liver. (E) A 3D volumetric render of *in vivo* spectral CT model top-ventral and bottom-lateral side of the heart and great vessel immediately after injection. (F) Top-heart and liver coronal view along the dotted line in (E), and bottom showing spleen, kidney, and inferior vena cava for the same. (G) Showing the sentinel lymph node mapping and resection in the *in vivo* model using spectral CT volumetric rendering after 2 h of intradermal injection of 100 μL of PEG-RITC-TaO_x colloidal suspension (210 mg mL^{-1}), yellow circle highlights the location of the lymph node. Reproduced from ref. 108 with permission from American Chemical Society, copyright 2011. Image assembled with **https://BioRender.com**.

9. Tungsten (74) nanoparticles

Tungsten (W) is known to be denser than iodine, and more recently, its role in biological systems was discovered in bacterial cells as an active binding site for enzymes.[84,109] Before the nano-form of tungsten could be used as a contrast agent, a solution of metals such as W, Yb, and Bi (10 mg mL^{-1}) were used for K-edge detection and image contrast enhancement.[110] The cuboidal trinuclear cluster of tungsten sulfide $(W_3S_4)^{4+}$ with TTHA ligand was investigated for X-ray CT contrast agent in early 2000.[111] Thereafter, poly ε-caprolactone-capped (tungsten oxide) WO_3 NPs proved to be efficient as contrast agents for X-ray CT imaging, and NPs were found to be non-toxic (*in vitro* study with HeLa and 4T1 breast cancer cells) and eliminated by an *in vivo* model within a few hours of administration.[112,113] *In vivo*, administration of 0.1 M nanoparticles in the mouse model confirmed that there was a contrast enhancement in the blood and other organs such as the liver, spleen, and kidney up to 24 h post-administration. The contrast enhancement of the blood showed a mono-exponential decay over time, which was due to the elimination of NPs. The results showed some retention of the NPs in the liver and spleen, along with the kidneys, which could be correlated to the renal excretion of NPs. The synthesized NPs showed improved retention (up to 2 h) which was significantly higher than that of iodine-based contrast agents (10 min), along with efficient removal, thus preventing adverse reactions. Another study used PEGylated WO_{3-x} NPs as effective CT contrast agents and photothermal therapy in a 4T1 tumor-bearing mouse model. The synthesized NPs effectively damaged tumor cells under a low-intensity NIR laser without affecting healthy cells. The nanoformulation showed great potential for use in photothermal therapy and tumor imaging with the help of SPCCT.[113]

10. Rhenium (75) nanoparticles

Another high-*Z* element, rhenium (Re), has gained interest over the last few years, where the nano-form of Re has been used for SPCCT imaging. Soesbe *et al.* compared the iodine and barium-based contrast agents with a colloidal form of tungsten, tantalum, and rhenium. The methylcellulose-stabilized nanopowder formulations were orally ingested by the *in vivo* model, followed by 2nd dose of the same contrast agent after 30 min. The study highlighted the advantage of the oral route over the intravenous administration of contrast agents in patients suffering from gastrointestinal bleeding, bowel ischemia, or Crohn's disease. The study also emphasized the potential of dual-layer DECT to distinguish between iodine and other high-*Z* element-based contrast agents in the colloidal form.[114]

A recent study used rhenium sulfide (ReS_2) nanoparticles as preclinical drugs for spectral CT imaging of the GI tract, along with CT-assisted photothermal therapy of tumors. The spectral

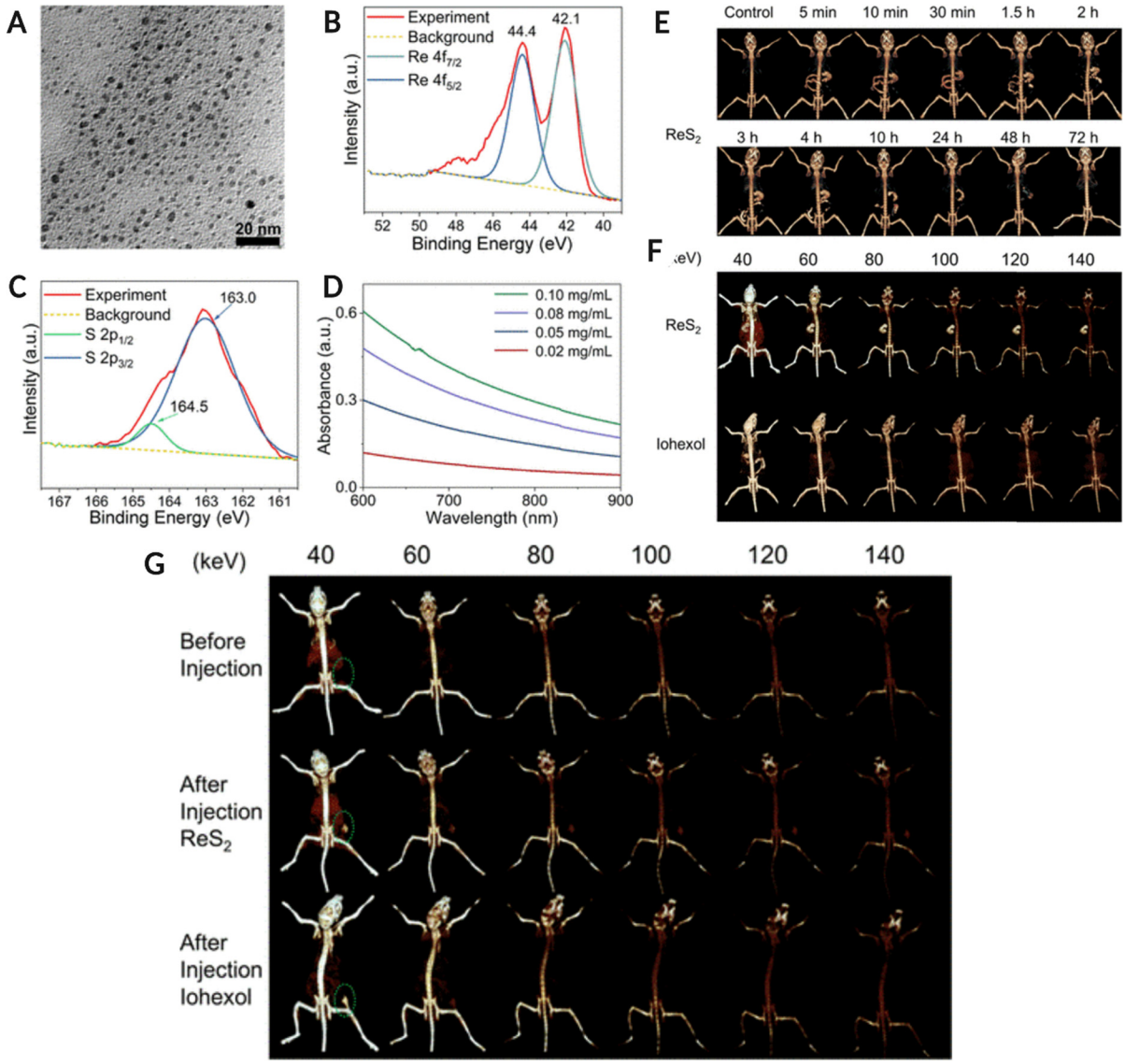

Fig. 9 (A–(D) Physico-chemical characterization of ReS_2 NPs. (A) TEM image of NPs, (B) Re 4f orbital XPS spectra, (C) S 2p orbital XPS spectra for ReS_2 NPs, and (D) UV-Vis-NIR absorbance spectra of Ns at different concentrations. (E) is conventional CT image of the GI tract of *in vivo* model fed with 400 μL, 10 mg mL^{-1} ReS_2 NPs colloid while (F) is the spectral CT image of the GI tract after 5 minutes of NPs and iohexol (400 μL, 35 mM) oral administration at different keV. (G) Spectral CT images of tumor-bearing mice pre and post-ReS_2 NPs (100 μL, 5 mg mL^{-1}, 17.5 mM Re) or iohexol (100 μL, 17.5 mM I) injection (tumor location highlighted with green circle). Reproduced from ref. 115 with permission from American Chemical Society, copyright 2019. Image assembled with **https://BioRender.com**.

CT imaging results confirmed that the ReS_2 NPs significantly enhanced the contrast relative to the background. Thus, ReS_2 NPs are good candidates for high-sensitivity spectral CT imaging for *in vivo* studies. Additionally, the ReS2 NPs were able to image the tumor *via* spectral CT post-administration in a 4T1 tumor-bearing mouse model. There was a significant improvement in contrast enhancement for the tumor, up to threefold upon nanoparticle injection, thus offering the possibility of disease diagnosis and therapy. In addition, when exposed to a low-intensity 808 nm laser, ReS_2 NPs were able to cause hyperthermia within the tumor environment, and complete eradication of the tumor was observed (Fig. 9).[115] The synthesized ReS_2 NPs demonstrated strong X-ray absorption at various energies for enhanced spectral CT imaging. This study also reported a significantly higher signal-to-noise ratio, thus offering a platform for theranostic applications without posing any safety concerns. Moreover, the biomedical imaging applications of Re-based nanostructures are not limited to spectral photon-counting CT imaging but have been explored for photoluminescence imaging, as reported elsewhere.[116] Fig. 9A–D shows the physicochemical characterization of ReS_2 NPs (TEM image, XPS analysis, and UV-Vis-NIR absorbance spectra) Fig. 9E is CT image of GI tract (*in vivo* model) using traditional CT system. The *in vivo* model consumed 400 μL of a 10 mg mL^{-1} ReS_2 NPs suspension. Fig. 9F shows the SPCCT image of the GI tract after oral administration of NPs and iohexol at different

energy levels. Fig. 9G represents the SPCCT images of tumor-bearing mice before and after ReS_2 NPs (100 μL, 5 mg mL^{-1}, 17.5 mM Re) or iohexol (100 μL, 17.5 mM I) injection (tumor location highlighted with green circle).

11. Other high-*Z* element nanoparticles

Other high-*Z* elements, either alone or in combination with other elements, have also been explored for diagnostic applications using SPCCT imaging. In an *in vitro* and *in vivo* study, dextran-functionalized nanoceria with a 17.5 nm hydrodynamic size accumulated at the inflammatory bowel disease site *in vivo* (external stimuli triggered colitis disease model) within 24 h of post-oral administration.[117] No CT contrast was observed in healthy mice after 24 h whereas significant attenuation was detected in the large intestines of mice with colitis. These results were corroborated by ICP-OES analysis, where no NPs were detected in any major organs in the healthy mouse, except small amounts in the stomach. However, in colitis mice, high levels of ceria were detected in the stomach and the small and large intestines. In contrast, colitis mice showed a significantly higher presence of NPs in the stomach and intestines (small and large). Additionally, approximately 97% of the administered formulation was cleared from the diseased animal within 24 h and showed no adverse effects on the accumulated sites. Another system that has been investigated includes the mixed-metal composition of nanosuspensions. The designed nanosystems consist of a nanotheranostic agent (Cu–Sb–S) coated with Au nanocrystals (Au@Cu–Sb–S) for multimodal imaging and phototherapy-enhanced radiotherapy. This system, when injected into 4T1 breast tumor-bearing mice *via* the tail vein, did not show any noticeable damage to healthy tissue, and photothermal therapy assisted in tumor eradication within 21 days. Furthermore, the Au@Cu–Sb–S NPs demonstrated superior X-ray attenuation and higher contrast than clinical iodine at 60, 100, and 140 keV at the tumor site at 24 h which was confirmed by photoacoustic imaging.[118]

12. Challenges, future scope, and conclusion

Spectral photon-counting CT imaging utilizing high-*Z*-element-based nanostructures has shown promising outcomes in biomedical imaging. However, the current limitations in exploring various shapes, sizes, and alloy/mixed-metal-based nanostructures for molecular imaging and diagnosis have not yet been fully investigated. Moreover, the focus has been primarily on a limited number of high-*Z* elements, leaving numerous high-*Z* element-based nanostructures unexplored. Nonetheless, the fields of nanotheranostics and nanotherapeutics are rapidly advancing, and we anticipate a surge in the number of nanostructures employed in the upcoming years. These advancements in technology will enable the prospect of personalized medicine to play a crucial role in defining the path for cancer and disease diagnosis, and therapeutics in the healthcare industry. To achieve this, significant efforts must be made to understand the short- and long-term implications of these high-*Z* element-based nanostructures on the intended patients as well as the environment. Detailed investigations related to their acute or chronic effects must be conducted in relevant animal models before these nanosystems can be considered viable options for diagnostic and/or therapeutic purposes. Another critical aspect while designing these NPs formulations is to ensure the degradability and/or excretion of NPs in the biological system. To date, there are limited studies exploring the potential excretion routes, as the primary focus has been on studying the bio-distribution and therapeutic responses of surface-engineered nanoparticulate formulations. One study reported that AuNPs with a core diameter of 25 nm which were intravenously injected in an *in vivo* model, accumulated preferentially in the liver with a small amount found in the lungs and spleen, and were flushed out *via* urine and feces routes.[119,120] The same excretory routes have been reported for manganese–gadolinium (Mn–Gd), tungsten disulphide (WS_2), and hafnium oxide (HfO_2) nanocolloid administered in different *in vivo* models for therapeutic applications as demonstrated by few studies.[121–123] Considering the potential cytotoxicity because of the accumulation of NPs in healthy tissues, the current and future nanotherapeutic or nanotheranostic formulations including both inorganic and organic systems must be critically characterized for cytotoxicity using respective *in vitro* models. Followed by efficacy, biodistribution, accumulation, degradability, and/or excretion pathway assessment using the *in vivo* models prior to clinical studies.[124]

The development of multimodality agents, as attractive as it may seem, needs to be thoroughly assessed from clinical and regulatory standpoints. Therefore, the major challenge is to engineer CT contrast agents that have a much higher contrast efficacy at different operating voltages and longer circulation times *in vivo* relative to clinical iodinated agents. The current formulations work well in small animal models; however, their translation into humans is still impossible. This is in part related to the potential CNR production *via* the beam-hardening effect, causing fewer photons below the K-edge energies of these elements to reach the detector. In this case, elements with higher atomic numbers produce a higher CNR. For example, this might lead to the contrast generation of tantalum being higher than that of ytterbium. All these limitations of the study can be addressed in the future in larger phantoms or animal models as the technology approaches the clinical stage of development. More recently, successful attempts have been performed by MARS bioimaging Ltd, New Zealand, using SPCCT by scanning the first human wrist and ankle (as shown in Fig. 1B) and generating clinically relevant images using the permissible clinical radiation doses. This demonstrates the potential of SPCCT as an imaging modality for human clinical trials.

Nanomaterials offer great potential for tuning the composition, shape, and targeting ligands, and early clinical diagnosis using spectral CT can be achieved. However, there are several challenges associated with nanoparticles, such as reproducible batch-to-batch synthesis, uniformity in properties, upscaling of

nanoparticle production, toxicity, and intrinsic properties that influence biodistribution, elimination, and target site accumulation. These limitations must be addressed to yield their intended translation into clinical diagnosis. The targeting ability of nanomaterials can be realized by surface modification of nanoparticles to make them target-specific and facilitate the binding and internalization in targeted cells with lower accumulation in non-specific and healthy tissues. With the advancement of medical diagnosis in the future, clinicians will be able to provide complete health checks rapidly and regularly in a non-invasive manner. Personalized medicine is a futuristic solution that would allow the design and administration of therapeutics based on the genetic makeup of a patient or person. Early detection or diagnosis based on genetic markers using a nanoparticulate approach for tailoring disease progression at the molecular level would incline the healthcare system towards preventive measures. Therefore, nanomaterials are expected to be used towards the development of platforms, supporting personalized medicine, and offering higher safety and better patient care at lower costs.

Author contributions

Isha Mutreja: conceptualization, literature review, writing – original draft. Nabil Maalej: conceptualization, literature review, writing – original draft. Ajeet Kaushik: conceptualization, writing – review & editing. Dhiraj Kumar: visualization, conceptualization, literature review, methodology, and writing – original draft. Aamir Raja: conceptualization, literature review, methodology, and writing – original draft.

Abbreviations

High-*Z*	High atomic number
CT	Computed tomography
FL	Fluorescence imaging
USG	Ultrasonography
US	Ultrasound
PET	Positron emission tomography
SPECT	Single photon emission tomography
MRI	Magnetic resonance imaging
PAT	Photoacoustic tomography
CT	Computed tomography
SPCCT	Spectral photon-counting CT
NPs	Nanoparticles
NRs	Nanorods
NSs	Nanostructures
NCs	Nanocrystals
DECT	Dual-energy CT
CNR	Contrast-to-noise ratio
MD	Material decomposition

Conflicts of interest

The authors have no conflicts of interest related to this work.

Acknowledgements

IM would like to acknowledge the Department of Restorative Sciences, School of Dentistry, University of Minnesota Start-up fund (1024-11462-20088-8008396). DK would like to thank the Department of Developmental and surgical sciences, School of Dentistry, University of Minnesota Start-up fund (1026-11434-20088-8008421). NM would like to thank Khalifa University of Science and Technology, Abu Dhabi, UAE for funding (account numbers: 8474000361 and 8474000366 (000160-Khalifa University-FSU). Also, some of the images were assembled and created with **BioRender.com**.

References

1 S. Hussain, I. Mubeen, N. Ullah, S. S. U. D. Shah, B. A. Khan, M. Zahoor, R. Ullah, F. A. Khan and M. A. Sultan, Modern Diagnostic Imaging Technique Applications and Risk Factors in the Medical Field: A Review, *Biomed. Res. Int.*, 2022, 1–19.

2 P. F. FitzGerald, R. E. Colborn, P. M. Edic, J. W. Lambert, A. S. Torres, P. J. Bonitatibus and B. M. Yeh, CT Image Contrast of High- Z Elements: Phantom Imaging Studies and Clinical Implications, *Radiology*, 2016, **278**, 723–733.

3 W. G. Bradley, History of Medical Imaging, *Proc. Am. Philos. Soc.*, 2008, **152**, 349–361.

4 E. Schena, C. Liguori, G. Frauenfelder, C. Massaroni, P. Saccomandi, F. Giurazza, F. Pitocco and R. Marano, Emerging clinical applications of computed tomography, *Med. Devices: Evidence Res.*, 2015, **8**, 265.

5 K. Cleary and T. M. Peters, Image-Guided Interventions: Technology Review and Clinical Applications, *Annu. Rev. Biomed. Eng.*, 2010, **12**, 119–142.

6 C. Zhang, L. Zhou, J. Zhang, R. Dai, P. Zhuang and Z. Ye, One-pot synthesis of flower-like Bi 2 S 3 nanoparticles for spectral CT imaging and photothermal therapy *in vivo*, *New J. Chem.*, 2022, **46**, 10458–10469.

7 D. P. Cormode, P. C. Naha and Z. A. Fayad, Nanoparticle contrast agents for computed tomography: A focus on micelles, *Contrast Media Mol. Imaging*, 2014, **9**, 37–52.

8 M. Moghiseh, E. Searle, D. Dixit, J. Kim, Y. C. Dong, D. P. Cormode, A. Butler and S. P. Gieseg, Spectral Photon-Counting CT Imaging of Gold Nanoparticle Labelled Monocytes for Detection of Atherosclerosis: A Preclinical Study, *Diagnostics*, 2023, **13**, 499.

9 M. Oumano, L. Russell, M. Salehjahromi, L. Shanshan, N. Sinha, W. Ngwa and H. Yu, CT imaging of gold nanoparticles in a human-sized phantom, *J. Appl. Clin. Med. Phys.*, 2021, **22**, 337–342.

10 J. Greffier, N. Villani, D. Defez, D. Dabli and S. Si-Mohamed, Spectral CT imaging: Technical principles of dual-energy CT and multi-energy photon-counting CT, *Diagn. Interv. Imaging*, 2023, **104**, 167–177.

11 F. Tatsugami, T. Higaki, Y. Nakamura, Y. Honda and K. Awai, Dual-energy CT: minimal essentials for radiologists, *Jpn. J. Radiol.*, 2022, **40**, 547–559.

12 C. H. McCollough, S. Leng, L. Yu and J. G. Fletcher, Dual- and Multi-Energy CT: Principles, Technical Approaches, and Clinical Applications, *Radiology*, 2015, **276**, 637–653.
13 A. P. Borges, C. Antunes and L. Curvo-Semedo, Pros and Cons of Dual-Energy CT Systems: ''One Does Not Fit All'', *Tomography*, 2023, **9**, 195–216.
14 J. Dudak, High-resolution X-ray imaging applications of hybrid-pixel photon counting detectors Timepix, *Radiat. Meas.*, 2020, **137**, 106409.
15 T. Stein, A. Rau, M. F. Russe, P. Arnold, S. Faby, S. Ulzheimer, M. Weis, M. F. Froelich, D. Overhoff, M. Horger, F. Hagen, M. Bongers, K. Nikolaou, S. O. Schönberg, F. Bamberg and J. Weiß, Photon-Counting Computed Tomography – Basic Principles, Potenzial Benefits, and Initial Clinical Experience, *RöFo - Fortschritte auf dem Gebiet der Röntgenstrahlen und der bildgebenden Verfahren*, 2023, **198**(8), 691–698.
16 T. Flohr and B. Schmidt, Technical Basics and Clinical Benefits of Photon-Counting CT, *Invest. Radiol.*, 2023, **58**(7), 441–450.
17 I. Bernabei, Y. Sayous, A. Y. Raja, M. R. Amma, A. Viry, S. Steinmetz, G. Falgayrac, R. B. Van Heeswijk, P. Omoumi, T. Pascart, L. K. Stamp, S. Nasi, T. Hügle, N. Busso, A. K. So and F. Becce, Multi-energy photon-counting computed tomography versus other clinical imaging techniques for the identification of articular calcium crystal deposition, *Rheumatology*, 2021, **60**(5), 2483–2485.
18 F. Becce, A. Viry, L. K. Stamp, T. Pascart, J. F. Budzik and A. Raja, Winds of change in imaging of calcium crystal deposition diseases, *Joint Bone Spine*, 2019, **86**(6), 665–668.
19 N. G. Anderson and A. P. Butler, Clinical applications of spectral molecular imaging: potential and challenges, *Contrast Media Mol. Imaging*, 2014, **9**, 3–12.
20 M. J. Willemink, M. Persson, A. Pourmorteza, N. J. Pelc and D. Fleischmann, Photon-counting CT: Technical Principles and Clinical Prospects, *Radiology*, 2018, **289**, 293–312.
21 M. Tortora, L. Gemini, I. D'Iglio, L. Ugga, G. Spadarella and R. Cuocolo, Spectral Photon-Counting Computed Tomography: A Review on Technical Principles and Clinical Applications, *J. Imaging*, 2022, **8**, 112.
22 J. P. Schlomka, E. Roessl, R. Dorscheid, S. Dill, G. Martens, T. Istel, C. Bäumer, C. Herrmann, R. Steadman, G. Zeitler, A. Livne and R. Proksa, Experimental feasibility of multi-energy photon-counting K-edge imaging in pre-clinical computed tomography, *Phys. Med. Biol.*, 2008, **53**, 4031–4047.
23 D. Pan, E. Roessl, J. Schlomka, S. D. Caruthers, A. Senpan, M. J. Scott, J. S. Allen, H. Zhang, G. Hu, P. J. Gaffney, E. T. Choi, V. Rasche, S. A. Wickline, R. Proksa and G. M. Lanza, Computed Tomography in Color: NanoK-Enhanced Spectral CT Molecular Imaging, *Angew. Chem., Int. Ed.*, 2010, **49**, 9635–9639.
24 D. Pan, C. O. Schirra, S. A. Wickline and G. M. Lanza, Multicolor computed tomographic molecular imaging with noncrystalline high-metal-density nanobeacons, *Contrast Media Mol. Imaging*, 2014, **9**, 13–25.
25 S. Si-Mohamed, D. Bar-Ness, M. Sigovan, V. Tatard-Leitman, D. P. Cormode, P. C. Naha, P. Coulon, L. Rascle, E. Roessl, M. Rokni, A. Altman, Y. Yagil, L. Boussel and P. Douek, Multicolour imaging with spectral photon-counting CT: a phantom study, *Eur. Radiol. Exp.*, 2018, **2**, 34.
26 W. A. Kalender, D. Kolditz, C. Steiding, V. Ruth, F. Lück, A.-C. Rößler and E. Wenkel, Technical feasibility proof for high-resolution low-dose photon-counting CT of the breast, *Eur. Radiol.*, 2017, **27**, 1081–1086.
27 S. Dahal, A. Y. Raja, E. Searle, F. E. Colgan, J. S. Crighton, J. Roake, L. Saba, S. Gieseg and A. P. H. Butler, Components of carotid atherosclerotic plaque in spectral photon-counting CT with histopathologic comparison, *Eur. Radiol.*, 2022, **33**, 1612–1619.
28 M. Kaur and V. Wasson, ROI Based Medical Image Compression for Telemedicine Application, *Procedia Comput. Sci.*, 2015, **70**, 579–585.
29 R. D. Badawi, H. Shi, P. Hu, S. Chen, T. Xu, P. M. Price, Y. Ding, B. A. Spencer, L. Nardo, W. Liu, J. Bao, T. Jones, H. Li and S. R. Cherry, First human imaging studies with the explorer total-body PET scanner, *J. Nucl. Med.*, 2019, **60**(3), 299–303.
30 A. Barbieri, M. L. Barretta, D. Rea, C. Picone, O. Fabozzi, G. Palma, L. Antonio, A. Federico, S. Bimonte, F. Setola, E. D. L. Castelguidone, M. Castellano, A. G. D'Errico, M. Caraglia and C. Arra, Intraluminal gel ultrasound and eco-color Doppler: New tools for the study of colorectal cancer in mice, *In Vivo*, 2013, **27**(4), 443–450.
31 Z. Chen, X. Mu, Z. Han, S. Yang, C. Zhang, Z. Guo, Y. Bai and W. He, An Optical/Photoacoustic Dual-Modality Probe: Ratiometric in/*ex Vivo* Imaging for Stimulated H2S Upregulation in Mice, *J. Am. Chem. Soc.*, 2019, **141**(45), 17973–17977.
32 G. A. Johnson, G. P. Cofer, S. L. Gewalt and L. W. Hedlund, Morphologic phenotyping with MR microscopy: The visible mouse, *Radiology*, 2002, **222**(3), 789–793.
33 MD INNOVATION TECH Applications MARS Spectral CT Scanner – MD INNOVATION TECH GmbH.
34 MARS bioimaging Applications & Publications – MARS bioimaging.
35 R. K. Panta, P. Carbonez, J. Damet, S. A. Adebileje, S. D. Alexander, M. R. Amma, M. Anjomrouz, F. Asghariomabad, A. Atharifard, K. Baer, B. Bamford, A. P. H. Butler, S. Bheesette, C. Chambers, A. I. Chernoglazov, S. Dahal, T. Dalefield, R. M. N. Doesburg, N. Duncan, S. P. Gieseg, S. Gurney, J. L. Healy, P. H. Butler, P. J. Hilton, P. Kanithi, T. Kirkbride, S. P. Lansley, C. Lowe, V. B. H. Mandalika, E. Marfo, A. Matanaghi, M. Moghiseh, D. Palmer, N. J. A. de Ruiter, H. M. Prebble, A. Y. Raja, M. Ramyar, P. Renaud, N. Schleich, E. Searle, M. Shamshad, J. S. Sheeja, R. Uddin, L. V. Broeke, S. T. Bell, V. S. Vivek, E. P. Walker, M. Wijesooriya, T. B. F. Woodfield, M. F. Walsh, R. M. N. Doesburg, A. I. Chernoglazov and B. P. Goulter, First human imaging with MARS photon-counting CT, 2018 IEEE Nuclear Science Symposium and Medical Imaging Conference Proceedings (NSS/MIC), IEEE, 2018, pp. 1–7.

36 Y. C. Dong, A. Kumar, D. N. Rosario-Berríos, S. Si-Mohamed, J. C. Hsu, L. M. Nieves, P. Douek, P. B. Noël and D. P. Cormode, Ytterbium Nanoparticle Contrast Agents for Conventional and Spectral Photon-Counting CT and Their Applications for Hydrogel Imaging, *ACS Appl. Mater. Interfaces*, 2022, **14**, 39274–39284.

37 S. Behzadi, V. Serpooshan, W. Tao, M. A. Hamaly, M. Y. Alkawareek, E. C. Dreaden, D. Brown, A. M. Alkilany, O. C. Farokhzad and M. Mahmoudi, Cellular uptake of nanoparticles: journey inside the cell, *Chem. Soc. Rev.*, 2017, **46**, 4218–4244.

38 M. J. Mitchell, M. M. Billingsley, R. M. Haley, M. E. Wechsler, N. A. Peppas and R. Langer, Engineering precision nanoparticles for drug delivery, *Nat. Rev. Drug Discovery*, 2021, **20**, 101–124.

39 R. Zein, W. Sharrouf and K. Selting, Physical Properties of Nanoparticles That Result in Improved Cancer Targeting, *J. Oncol.*, 2020, **2020**, 1–16.

40 O. Harush-Frenkel, N. Debotton, S. Benita and Y. Altschuler, Targeting of nanoparticles to the clathrin-mediated endocytic pathway, *Biochem. Biophys. Res. Commun.*, 2007, **353**, 26–32.

41 J. A. Swanson, Shaping cups into phagosomes and macropinosomes, *Nat. Rev. Mol. Cell Biol.*, 2008, **9**, 639–649.

42 G. J. Doherty and H. T. McMahon, Mechanisms of Endocytosis, *Annu. Rev. Biochem.*, 2009, **78**, 857–902.

43 G. Sahay, D. Y. Alakhova and A. V. Kabanov, Endocytosis of nanomedicines, *J. Controlled Release*, 2010, **145**, 182–195.

44 D. A. Kuhn, D. Vanhecke, B. Michen, F. Blank, P. Gehr, A. Petri-Fink and B. Rothen-Rutishauser, Different endocytotic uptake mechanisms for nanoparticles in epithelial cells and macrophages, *Beilstein J. Nanotechnol.*, 2014, **5**, 1625–1636.

45 M. Mahmoudi, A. Tachibana, A. B. Goldstone, Y. J. Woo, P. Chakraborty, K. R. Lee, C. S. Foote, S. Piecewicz, J. C. Barrozo, A. Wakeel, B. W. Rice, C. B. Bell III and P. C. Yang, Novel MRI Contrast Agent from Magnetotactic Bacteria Enables *In Vivo* Tracking of iPSC-derived Cardiomyocytes, *Sci. Rep.*, 2016, **6**, 26960.

46 P. Sabourian, G. Yazdani, S. S. Ashraf, M. Frounchi, S. Mashayekhan, S. Kiani and A. Kakkar, Effect of Physico-Chemical Properties of Nanoparticles on Their Intracellular Uptake, *Int. J. Mol. Sci.*, 2020, **21**, 8019.

47 O. L. McGovern, Y. Rivera-Cuevas and V. B. Carruthers, Emerging Mechanisms of Endocytosis in Toxoplasma gondii, *Life*, 2021, **11**, 84.

48 R. Bilardo, F. Traldi, A. Vdovchenko and M. Resmini, Influence of surface chemistry and morphology of nanoparticles on protein corona formation, *Wiley Interdiscip. Rev.: Nanomed. Nanobiotechnol.*, 2022, **14**(4), e1788.

49 J. C. Hsu, L. M. Nieves, O. Betzer, T. Sadan, P. B. Noël, R. Popovtzer and D. P. Cormode, Nanoparticle contrast agents for X-ray imaging applications, *Wiley Interdiscip. Rev.: Nanomed. Nanobiotechnol.*, 2020, **12**(6), e1642.

50 L. Zheng, R. Zhu, L. Chen, Q. Fu, J. Li, C. Chen, J. Song and H. Yang, X-ray sensitive high-Z metal nanocrystals for cancer imaging and therapy, *Nano Res.*, 2021, **14**, 3744–3755.

51 J. Kim, D. Bar-Ness, S. Si-Mohamed, P. Coulon, I. Blevis, P. Douek and D. P. Cormode, Assessment of candidate elements for development of spectral photon-counting CT specific contrast agents, *Sci. Rep.*, 2018, **8**, 12119.

52 M. Berger, Q. Yang and A. Maier, *Medical Imaging Systems: An Introductory Guide*, Springer, 2018, p. 11111.

53 A. Detappe, F. Lux and O. Tillement, Pushing radiation therapy limitations with theranostic nanoparticles, *Nanomedicine*, 2016, **11**, 997–999.

54 S.-W. Chou, Y.-H. Shau, P.-C. Wu, Y.-S. Yang, D.-B. Shieh and C.-C. Chen, *In Vitro* and *in Vivo* Studies of FePt Nanoparticles for Dual Modal CT/MRI Molecular Imaging, *J. Am. Chem. Soc.*, 2010, **132**, 13270–13278.

55 N. Halttunen, F. Lerouge, F. Chaput, M. Vandamme, S. Karpati, S. Si-Mohamed, M. Sigovan, L. Boussel, E. Chereul, P. Douek and S. Parola, Hybrid Nano-GdF3 contrast media allows pre-clinical *in vivo* element-specific K-edge imaging and quantification, *Sci. Rep.*, 2019, **9**, 12090.

56 S. Si-Mohamed, V. Tatard-Leitman, A. Laugerette, M. Sigovan, D. Pfeiffer, E. J. Rummeny, P. Coulon, Y. Yagil, P. Douek, L. Boussel and P. B. Noël, Spectral Photon-Counting Computed Tomography (SPCCT): in-vivo single-acquisition multi-phase liver imaging with a dual contrast agent protocol, *Sci. Rep.*, 2019, **9**, 8458.

57 B. M. Yeh, P. F. FitzGerald, P. M. Edic, J. W. Lambert, R. E. Colborn, M. E. Marino, P. M. Evans, J. C. Roberts, Z. J. Wang, M. J. Wong and P. J. Bonitatibus, Opportunities for new CT contrast agents to maximize the diagnostic potential of emerging spectral CT technologies, *Adv. Drug Deliv. Rev.*, 2017, **113**, 201–222.

58 P. He, B. Wei, P. Feng, M. Chen and D. Mi, Material Discrimination Based on K-edge Characteristics, *Comput. Math. Methods Med.*, 2013, **2013**, 1–6.

59 S. A. Si-Mohamed, M. Sigovan, J. C. Hsu, V. Tatard-Leitman, L. Chalabreysse, P. C. Naha, T. Garrivier, R. Dessouky, M. Carnaru, L. Boussel, D. P. Cormode and P. C. Douek, *In Vivo* Molecular K-Edge Imaging of Atherosclerotic Plaque Using Photon-counting CT, *Radiology*, 2021, **300**, 98–107.

60 I. Riederer, D. Bar-Ness, M. A. Kimm, S. Si-Mohamed, P. B. Noël, E. J. Rummeny, P. Douek and D. Pfeiffer, Liquid Embolic Agents in Spectral X-Ray Photon-Counting Computed Tomography using Tantalum K-Edge Imaging, *Sci. Rep.*, 2019, **9**, 5268.

61 F. Ostadhossein, I. Tripathi, L. Benig, D. LoBato, M. Moghiseh, C. Lowe, A. Raja, A. Butler, R. Panta, M. Anjomrouz, A. Chernoglazov and D. Pan, Multi-''Color'' Delineation of Bone Microdamages Using Ligand-Directed Sub-5 nm Hafnia Nanodots and Photon Counting CT Imaging, *Adv. Funct. Mater.*, 2020, **30**, 1904936.

62 P. Singh, S. Pandit, V. R. S. S. Mokkapati, A. Garg, V. Ravikumar and I. Mijakovic, Gold Nanoparticles in Diagnostics and Therapeutics for Human Cancer, *Int. J. Mol. Sci.*, 2018, **19**, 1979.

63 M. Moghiseh, C. Lowe, J. G. Lewis, D. Kumar, A. Butler, N. Anderson, A. Raja and A. Bombonati, Spectral Photon-Counting Molecular Imaging for Quantification of

Monoclonal Antibody-Conjugated Gold Nanoparticles Targeted to Lymphoma and Breast Cancer: An *in Vitro* Study, *Contrast Media Mol. Imaging*, 2018, **2018**, 2136840.

64 M. A. Kimm, M. Shevtsov, C. Werner, W. Sievert, W. Zhiyuan, O. Schoppe, B. H. Menze, E. J. Rummeny, R. Proksa, O. Bystrova, M. Martynova, G. Multhoff and S. Stangl, Gold Nanoparticle Mediated Multi-Modal CT Imaging of Hsp70 Membrane-Positive Tumors, *Cancers*, 2020, **12**, 1331.

65 M. Moghiseh, A. Raja, D. Kumar, R. Panta, J. L. Healy, J. Lewis, A. I. Chernoglazov, C. Lowe, A. Butler, S. A. Adebileje, S. D. Alexander, M. R. Amma, M. Anjomrouz, F. Asghariomabad, A. Atharifard, K. Baer, B. Bamford, S. T. Bell, S. Bheesette, P. H. Butler, P. Carbonez, C. Chambers, S. Dahal, T. Dalefield, J. Damet, N. J. A. de Ruiter, R. M. N. Doesburg, N. Duncan, S. P. Gieseg, B. P. Goulter, S. Gurney, P. J. Hilton, P. Kanithi, T. Kirkbride, S. P. Lansley, V. B. H. Mandalika, E. Marfo, A. Matanaghi, D. Palmer, H. M. Prebble, M. Ramyar, P. Renaud, N. Schleich, E. Searle, M. Shamshad, J. S. Sheeja, R. Uddin, L. V. Broeke, P. Walker, M. F. Walsh, M. Wijesooriya, T. B. F. Woodfield and N. Anderson Cancer Imaging with Nanoparticles Using MARS Spectral Scanner, 2018 IEEE Nuclear Science Symposium and Medical Imaging Conference Proceedings (NSS/MIC), IEEE, pp. 1–4.

66 D. Kumar, I. Mutreja, K. Chitcholtan and P. Sykes, Cytotoxicity and cellular uptake of different sized gold nanoparticles in ovarian cancer cells, *Nanotechnology*, 2017, **28**, 475101.

67 D. Kumar, M. Moghiseh, K. Chitcholtan, I. Mutreja, C. Lowe, A. Kaushik, A. Butler, P. Sykes, N. Anderson and A. Raja, LHRH conjugated gold nanoparticles assisted efficient ovarian cancer targeting evaluated *via* spectral photon-counting CT imaging: a proof-of-concept research, *J. Mater. Chem. B*, 2023, **11**, 1916–1928.

68 J. R. Ashton, K. D. Castle, Y. Qi, D. G. Kirsch, J. L. West and C. T. Badea, Dual-Energy CT Imaging of Tumor Liposome Delivery After Gold Nanoparticle-Augmented Radiation Therapy, *Theranostics*, 2018, **8**, 1782–1797.

69 S. Khademi, S. Sarkar, A. Shakeri-Zadeh, N. Attaran, S. Kharrazi, R. Solgi, M. Reza Ay, H. Azimian and H. Ghadiri, Dual-energy CT imaging of nasopharyngeal cancer cells using multifunctional gold nanoparticles, *IET Nanobiotechnol.*, 2019, **13**, 957–961.

70 D. P. Cormode, E. Roessl, A. Thran, T. Skajaa, R. E. Gordon, J.-P. Schlomka, V. Fuster, E. A. Fisher, W. J. M. Mulder, R. Proksa and Z. A. Fayad, Atherosclerotic plaque composition: Analysis with multicolor CT and targeted gold nanoparticles, *Radiology*, 2010, **256**, 774–782.

71 S. Si-Mohamed, D. P. Cormode, D. Bar-Ness, M. Sigovan, P. C. Naha, J.-B. Langlois, L. Chalabreysse, P. Coulon, I. Blevis, E. Roessl, K. Erhard, L. Boussel and P. Douek, Evaluation of spectral photon counting computed tomography K-edge imaging for determination of gold nanoparticle biodistribution *in vivo*, *Nanoscale*, 2017, **9**, 18246–18257.

72 E. Cuccione, P. Chhour, S. Si-Mohamed, C. Dumot, J. Kim, V. Hubert, C. C. Da Silva, M. Vandamme, E. Chereul, J. Balegamire, Y. Chevalier, Y. Berthezène, L. Boussel, P. Douek, D. P. Cormode and M. Wiart, Multicolor spectral photon counting CT monitors and quantifies therapeutic cells and their encapsulating scaffold in a model of brain damage, *Nanotheranostics*, 2020, **4**, 129–141.

73 D. Wan, D. Chen, K. Li, Y. Qu, K. Sun, K. Tao, K. Dai and S. Ai, Gold Nanoparticles as a Potential Cellular Probe for Tracking of Stem Cells in Bone Regeneration Using Dual-Energy Computed Tomography, *ACS Appl. Mater. Interfaces*, 2016, **8**, 32241–32249.

74 D. P. Cormode, S. Si-Mohamed, D. Bar-Ness, M. Sigovan, P. C. Naha, J. Balegamire, F. Lavenne, P. Coulon, E. Roessl, M. Bartels, M. Rokni, I. Blevis, L. Boussel and P. Douek, Multicolor spectral photon-counting computed tomography: *In vivo* dual contrast imaging with a high count rate scanner, *Sci. Rep.*, 2017, **7**, 4784.

75 Y. C. Dong, M. Hajfathalian, P. S. N. Maidment, J. C. Hsu, P. C. Naha, S. Si-Mohamed, M. Breuilly, J. Kim, P. Chhour, P. Douek, H. I. Litt and D. P. Cormode, Effect of Gold Nanoparticle Size on Their Properties as Contrast Agents for Computed Tomography, *Sci. Rep.*, 2019, **9**, 14912.

76 P. C. Zambrano-Rodríguez, S. Bolaños-Puchet, H. J. Reyes-Alva, L. E. García-Orozco, M. E. Romero-Piña, A. Martinez-Cruz, G. Guízar-Sahagún and L. A. Medina, Micro-CT myelography using contrast-enhanced digital subtraction: feasibility and initial results in healthy rats, *Neuroradiology*, 2019, **61**, 323–330.

77 M. Sadeghian, P. Akhlaghi and A. Mesbahi, Investigation of imaging properties of novel contrast agents based on gold, silver and bismuth nanoparticles in spectral computed tomography using Monte Carlo simulation, *Polish J. Medical Phys. Eng.*, 2020, **26**, 21–29.

78 B. D. Jo, S.-J. Park, H. M. Kim, D. H. Kim and H.-J. Kim, Spectral computed tomography for quantitative decomposition of vulnerable plaques using a dual-energy technique: a Monte Carlo simulation study, *J. Instrum.*, 2016, **11**, P02011.

79 M. Sadeghian, P. Akhlaghi and A. Mesbahi, Investigation of imaging properties of novel contrast agents based on gold, silver and bismuth nanoparticles in spectral computed tomography using Monte Carlo simulation, *Polish J. Medical Phys. Eng.*, 2020, **26**, 21–29.

80 S. Si-Mohamed, A. Thivolet, P.-E. Bonnot, D. Bar-Ness, V. Képénékian, D. P. Cormode, P. Douek and P. Rousset, Improved Peritoneal Cavity and Abdominal Organ Imaging Using a Biphasic Contrast Agent Protocol and Spectral Photon Counting Computed Tomography K-Edge Imaging, *Invest. Radiol.*, 2018, **53**, 629–639.

81 A. Ranga, Y. Agarwal and K. J. Garg, Gadolinium based contrast agents in current practice: Risks of accumulation and toxicity in patients with normal renal function, *Indian J. Radiol. Imaging*, 2017, **27**(2), 141–147.

82 R. Marasini, T. D. Thanh Nguyen and S. Aryal, Integration of gadolinium in nanostructure for contrast enhanced-magnetic

resonance imaging, *Wiley Interdiscip. Rev.: Nanomed. Nanobiotechnol.*, 2020, **12**(1), e1580.

83 P. D. Nallathamby, K. Cowden-Dahl and R. K. Roeder, Modular nanoparticle probes for personalized *in vitro* and *in vivo* imaging of cancer cell populations, *Advanced Materials – TechConnect Briefs 2017*, 2017, vol. 3.

84 W. He, K. Ai and L. Lu, Nanoparticulate X-ray CT contrast agents, *Sci. China: Chem.*, 2015, **58**, 753–760.

85 O. Kochebina, A. Halty, J. Taleb, D. K. David Kryza, M. Janier, A. B. Sadr, C. Mory, D. Bar-Ness, P. Douek, T. Baudier, S. Rit and D. Sarrut Quantification of Gd-Nanoparticles Concentration with SPECT and Spectral Photon Counting CT (CREATIS-CNRS UMR 5220, INSERM U1206, Universite Lyon 1 INSA Lyon, Universite Jean Monnet Saint-Etienne, 7 Avenue Jean Capelle, Villeurbanne, 69100, France: Institute of Electrical and Electronics Engineers Inc.), 2018.

86 C. T. Badea, M. Holbrook, D. P. Clark and K. Ghaghada, Spectral imaging of iodine and gadolinium nanoparticles using dual-energy CT, in *Progress in Biomedical Optics and Imaging Proceedings of SPIE*, 2018, vol. 10573, DOI: 10.1117/12.2293625.

87 S. Wu, X. Meng, X. Jiang, Y. Wu, S. Zhai, X. Wang, Y. Liu, J. Zhang, X. Zhao, Y. Zhou, W. Bu and Z. Yao, Harnessing X-Ray Energy-Dependent Attenuation of Bismuth-Based Nanoprobes for Accurate Diagnosis of Liver Fibrosis, *Adv. Sci.*, 2021, **8**, 2002548.

88 M. Sadeghian and A. Mesbahi, Imaging properties of Fe3O4@Au and Fe3O4@Bi hybrid nanocomposites as contrast agents in spectral X-ray computed tomography: A Monte Carlo simulation study, *Nanomed. J.*, 2021, **8**, 220–228.

89 C. Zwicker, M. Hering and R. Langer, Computed tomography with iodine-free contrast media, *Eur. Radiol.*, 1997, **7**, 1123–1126.

90 E. Unger and F. Gutierrez, Ytterbium-DTPA A Potential Intravascular Contrast Agent, *Invest. Radiol.*, 1986, **21**, 802–807.

91 Y. Liu, K. Ai, J. Liu, Q. Yuan, Y. He and L. Lu, A High-Performance Ytterbium-Based Nanoparticulate Contrast Agent for *In Vivo* X-Ray Computed Tomography Imaging, *Angew. Chem., Int. Ed.*, 2012, **51**, 1437–1442.

92 Z. Liu, Z. Li, J. Liu, S. Gu, Q. Yuan, J. Ren and X. Qu, Long-circulating Er3 + -doped Yb2O3 up-conversion nanoparticle as an *in vivo* X-Ray CT imaging contrast agent, *Biomaterials*, 2012, **33**, 6748–6757.

93 D. Pan, C. O. Schirra, A. Senpan, A. H. Schmieder, A. J. Stacy, E. Roessl, A. Thran, S. A. Wickline, R. Proska and G. M. Lanza, An Early Investigation of Ytterbium Nanocolloids for Selective and Quantitative ''Multicolor'' Spectral CT Imaging, *ACS Nano*, 2012, **6**, 3364–3370.

94 Y. C. Dong, A. Kumar, D. N. Rosario-Berríos, S. Si-Mohamed, J. C. Hsu, L. M. Nieves, P. Douek, P. B. Noël and D. P. Cormode, Ytterbium Nanoparticle Contrast Agents for Conventional and Spectral Photon-Counting CT and Their Applications for Hydrogel Imaging, *ACS Appl. Mater. Interfaces*, 2022, **14**, 39274–39284.

95 W. Krause, G. Schuhmann-Giampieri, M. Bauer, W.-R. Press and P. Muschick, Ytterbium- and Dysprosium-EOB-DTPA, *Invest. Radiol.*, 1996, **31**, 502–511.

96 S. A. Schmitz, S. Wagner, G. Schuhmann-Giampieri, W. Krause, M. Bollow and K. J. Wolf, Gd-EOB-DTPA and Yb-EOB-DTPA: two prototypic contrast media for CT detection of liver lesions in dogs, *Radiology*, 1997, **205**, 361–366.

97 L. Xiong, T. Yang, Y. Yang, C. Xu and F. Li, Long-term *in vivo* biodistribution imaging and toxicity of polyacrylic acid-coated upconversion nanophosphors, *Biomaterials*, 2010, **31**, 7078–7085.

98 Y. Wang, C. Jiang, W. He, K. Ai, X. Ren, L. Liu, M. Zhang and L. Lu, Targeted Imaging of Damaged Bone *in Vivo* with Gemstone Spectral Computed Tomography, *ACS Nano*, 2016, **10**, 4164–4172.

99 H. Xing, W. Bu, Q. Ren, X. Zheng, M. Li, S. Zhang, H. Qu, Z. Wang, Y. Hua, K. Zhao, L. Zhou, W. Peng and J. Shi, A NaYbF4: Tm3+ nanoprobe for CT and NIR-to-NIR fluorescent bimodal imaging, *Biomaterials*, 2012, **33**, 5384–5393.

100 Y. Liu, K. Ai, J. Liu, Q. Yuan, Y. He and L. Lu, Hybrid BaYbF 5 Nanoparticles: Novel Binary Contrast Agent for High-Resolution *in Vivo* X-ray Computed Tomography Angiography, *Adv. Healthc. Mater.*, 2012, **1**, 461–466.

101 Y. Sebti, S. Si-Mohamed, R. Aid, F. Geinguenaud, M. Chalal, Y. Lalatonne, F. Chaubet, P. Ou and L. Motte, Optical and X-ray attenuation properties of hafnium oxide nanoparticles surface functionalized with fucoidan: toward the early diagnosis of atherothrombotic diseases, *Mater. Adv.*, 2023, **4**, 1011–1020.

102 F. Ostadhossein, P. Moitra, N. Gunaseelan, M. Nelappana, C. Lowe, M. Moghiseh, A. Butler, N. de Ruiter, H. Mandalika, I. Tripathi, S. K. Misra and D. Pan, Hitchhiking probiotic vectors to deliver ultra-small hafnia nanoparticles for 'Color' gastrointestinal tract photon counting X-ray imaging, *Nanoscale Horiz.*, 2022, **7**, 533–542.

103 T. L. McGinnity, O. Dominguez, T. E. Curtis, P. D. Nallathamby, A. J. Hoffman and R. K. Roeder, Hafnia (HfO 2) nanoparticles as an X-ray contrast agent and mid-infrared biosensor, *Nanoscale*, 2016, **8**, 13627–13637.

104 P. D. Nallathamby, T. L. Mcginnity, L. E. Cole, M. E. Best, T. Vargo-Gogola and R. K. Roeder, Design and Synthesis of Nanoparticle Contrast Agents for Spectral (color) X-Ray Imaging, *MRS Proc.*, 2015, **1719**, mrsf14-1719-c05-08.

105 N. Wang, H. Li, J. Wang, S. Chen, Y. Ma and Z. Zhang, Study on the Anticorrosion, Biocompatibility, and Osteoinductivity of Tantalum Decorated with Tantalum Oxide Nanotube Array Films, *ACS Appl. Mater. Interfaces*, 2012, **4**, 4516–4523.

106 P. J. Bonitatibus, Jr., A. S. Torres, G. D. Goddard, P. F. FitzGerald and A. M. Kulkarni, Synthesis, characterization, and computed tomography imaging of a tantalum oxide nanoparticle imaging agent, *Chem. Commun.*, 2010, **46**, 8956.

107 P. J. Bonitatibus, A. S. Torres, B. Kandapallil, B. D. Lee, G. D. Goddard, R. E. Colborn and M. E. Marino, Preclinical Assessment of a Zwitterionic Tantalum Oxide Nanoparticle X-ray Contrast Agent, *ACS Nano*, 2012, **6**, 6650–6658.

108 M. H. Oh, N. Lee, H. Kim, S. P. Park, Y. Piao, J. Lee, S. W. Jun, W. K. Moon, S. H. Choi and T. Hyeon, Large-Scale Synthesis of Bioinert Tantalum Oxide Nanoparticles for X-ray Computed Tomography Imaging and Bimodal Image-Guided Sentinel Lymph Node Mapping, *J. Am. Chem. Soc.*, 2011, **133**, 5508–5515.

109 C. S. Seelmann, M. Willistein, J. Heider and M. Boll, Tungstoenzymes: Occurrence, Catalytic Diversity and Cofactor Synthesis, *Inorganics*, 2020, **8**, 44.

110 C. Amato, Novel Contrast Agents in Photon-Counting Computed Tomography – heiDOK, 2022.

111 S.-B. Yu, M. Droege, B. Segal, S.-H. Kim, T. Sanderson and A. D. Watson, Cuboidal W 3 S 4 Cluster Complexes as New Generation X-ray Contrast Agents, *Inorg. Chem.*, 2000, **39**, 1325–1328.

112 A. Jakhmola, N. Anton, H. Anton, N. Messaddeq, F. Hallouard, A. Klymchenko, Y. Mely and T. F. Vandamme, Poly-ε-caprolactone tungsten oxide nanoparticles as a contrast agent for X-ray computed tomography, *Biomaterials*, 2014, **35**, 2981–2986.

113 J. Liu, J. Han, Z. Kang, R. Golamaully, N. Xu, H. Li and X. Han, *In vivo* near-infrared photothermal therapy and computed tomography imaging of cancer cells using novel tungsten-based theranostic probe, *Nanoscale*, 2014, **6**, 5770.

114 T. C. Soesbe, M. A. Lewis, K. Nasr, L. Ananthakrishnan and R. E. Lenkinski, Separating High-Z Oral Contrast From Intravascular Iodine Contrast in an Animal Model Using Dual-Layer Spectral CT, *Acad. Radiol.*, 2019, **26**, 1237–1244.

115 X. Wang, J. Wang, J. Pan, F. Zhao, D. Kan, R. Cheng, X. Zhang and S.-K. Sun, Rhenium Sulfide Nanoparticles as a Biosafe Spectral CT Contrast Agent for Gastrointestinal Tract Imaging and Tumor Theranostics *in Vivo*, *ACS Appl. Mater. Interfaces*, 2019, **11**, 33650–33658.

116 Y. Li, Z. Luo, Y. Song, Y. Yuan, X. Peng, J. Song and J. Qu, Rhenium disulfide nanosheets as a promising probe for intracellular two-photon luminescence imaging, *Sens. Actuators, B*, 2022, **362**, 131781.

117 P. C. Naha, J. C. Hsu, J. Kim, S. Shah, M. Bouché, S. Si-Mohamed, D. N. Rosario-Berrios, P. Douek, M. Hajfathalian, P. Yasini, S. Singh, M. A. Rosen, M. A. Morgan and D. P. Cormode, Dextran-Coated Cerium Oxide Nanoparticles: A Computed Tomography Contrast Agent for Imaging the Gastrointestinal Tract and Inflammatory Bowel Disease, *ACS Nano*, 2020, **14**, 10187–10197.

118 H. Hu, S. Zheng, M. Hou, K. Zhu, C. Chen, Z. Wu, L. Qi, Y. Ren, B. Wu, Y. Xu, C. Yan and B. Zhao, Functionalized Au@Cu-Sb-S Nanoparticles for Spectral CT/Photoacoustic Imaging-Guided Synergetic Photo-Radiotherapy in Breast Cancer, *Int. J. Nanomed.*, 2022, **17**, 395–407.

119 N. Hadrup, A. K. Sharma, M. Poulsen and E. Nielsen, Toxicological risk assessment of elemental gold following oral exposure to sheets and nanoparticles - A review, *Regul. Toxicol. Pharmacol.*, 2015, **72**(2), 216–221.

120 M. Bednarski, M. Dudek, J. Knutelska, L. Nowiński, J. Sapa, M. Zygmunt, G. Nowak, M. Luty-Błocho, M. Wojnicki, K. Fitzner and M. Tęsiorowski, The influence of the route of administration of gold nanoparticles on their tissue distribution and basic biochemical parameters: *In vivo* studies, *Pharmacol. Rep.*, 2015, **67**(3), 405–409.

121 K. Wang, D. Pan, A. H. Schmieder, A. Senpan, S. D. Caruthers, G. Cui, J. S. Allen, H. Zhang, B. Shen and G. M. Lanza, Atherosclerotic neovasculature MR imaging with mixed manganese-gadolinium nanocolloids in hyperlipidemic rabbits, *Nanomedicine*, 2015, **11**(3), 569–578.

122 A. Surendranath, Evaluation of biodistribution and kinetics of tungsten disulphide quantum dots by Inductively coupled plasma mass spectroscopy: A detailed *in vivo* QD-bio interactions study, *Colloids Surf., B*, 2023, **223**, 113153.

123 Y. Li, Y. Qi, H. Zhang, Z. Xia, T. Xie, W. Li, D. Zhong, H. Zhu and M. Zhou, Gram-scale synthesis of highly biocompatible and intravenous injectable hafnium oxide nanocrystal with enhanced radiotherapy efficacy for cancer theranostic, *Biomaterials*, 2020, **226**, 119538.

124 L. K. Bogart, G. Pourroy, C. J. Murphy, V. Puntes, T. Pellegrino, D. Rosenblum, D. Peer and R. Lévy, Nanoparticles for Imaging, Sensing, and Therapeutic Intervention, *ACS Nano*, 2014, **8**, 3107–3122.